

# HP1 reshapes nucleosome core to promote phase separation of heterochromatin

<https://doi.org/10.1038/s41586-019-1669-2>

Received: 8 November 2018

Accepted: 17 September 2019

Published online: 16 October 2019

S. Sanulli<sup>1</sup>, M. J. Trnka<sup>1</sup>, V. Dharmarajan<sup>2</sup>, R. W. Tibble<sup>1,3</sup>, B. D. Pascal<sup>2</sup>, A. L. Burlingame<sup>1</sup>, P. R. Griffin<sup>2</sup>, J. D. Gross<sup>1\*</sup> & G. J. Narlikar<sup>4\*</sup>

Heterochromatin affects genome function at many levels. It enables heritable gene repression, maintains chromosome integrity and provides mechanical rigidity to the nucleus<sup>1,2</sup>. These diverse functions are proposed to arise in part from compaction of the underlying chromatin<sup>2</sup>. A major type of heterochromatin contains at its core the complex formed between HP1 proteins and chromatin that is methylated on histone H3, lysine 9 (H3K9me). HP1 is proposed to use oligomerization to compact chromatin into phase-separated condensates<sup>3–6</sup>. Yet, how HP1-mediated phase separation relates to chromatin compaction remains unclear. Here we show that chromatin compaction by the *Schizosaccharomyces pombe* HP1 protein Swi6 results in phase-separated liquid condensates. Unexpectedly, we find that Swi6 substantially increases the accessibility and dynamics of buried histone residues within a nucleosome. Restraining these dynamics impairs compaction of chromatin into liquid droplets by Swi6. Our results indicate that Swi6 couples its oligomerization to the phase separation of chromatin by a counterintuitive mechanism, namely the dynamic exposure of buried nucleosomal regions. We propose that such reshaping of the octamer core by Swi6 increases opportunities for multivalent interactions between nucleosomes, thereby promoting phase separation. This mechanism may more generally drive chromatin organization beyond heterochromatin.

Swi6 has two structured domains, the chromodomain, which binds the H3K9me mark, and the chromoshadow domain (CSD), which forms a dimer and contributes to nucleosome binding<sup>4,7</sup> (Fig. 1a, Extended Data Fig. 1a). The chromodomain and CSD are connected by a hinge region that binds DNA in a sequence non-specific manner<sup>7</sup>. Previous studies showed four molecules of Swi6 can bind to a single H3K9me nucleosome and we find dinucleosomes bind at least seven Swi6 molecules<sup>3</sup> (Extended Data Fig. 1b–e).

To understand the mechanism of Swi6 action, we probed how Swi6 engages a mononucleosome using cross-linking mass spectrometry (XLMS). We used nucleosomes containing a methyl lysine analogue on H3K9 (H3K9me3 nucleosomes)<sup>4</sup> (Fig. 1b, Extended Data Fig. 2a–d). In addition to cross-links between the chromodomain and H3, we obtained extensive cross-links between the Swi6 CSD and the octamer core, particularly H2B (Fig. 1b, Extended Data Fig. 2d). The CSD–CSD dimer interface is known to interact with proteins containing the motif  $\phi X(V/P)X\phi$  (in which  $\phi$  and X indicate a hydrophobic and any amino acid, respectively)<sup>8,9</sup>. The CSD of mammalian HP1 proteins has been shown to interact with the H3 $\alpha$ N helix region of the nucleosome core<sup>10,11</sup>. However, the CSD of Swi6 does not interact substantially with the H3 $\alpha$ N helix region and we do not observe crosslinks between the Swi6 CSD and the H3 $\alpha$ N region<sup>9</sup>. Instead, we detect cross-linking between the Swi6 CSD and the  $\alpha$ 1-helix of H2B, which also contains a  $\phi X(V/P)X\phi$  motif (Extended Data Fig. 2c, d). Using <sup>1</sup>H–<sup>15</sup>N heteronuclear single

quantum coherence (HSQC) NMR we found that binding of the H2B peptide containing the  $\phi X(V/P)X\phi$  motif (residues 36–54) causes chemical shift perturbations in the CSD cleft indicating a direct interaction<sup>9</sup> (Fig. 1c, Extended Data Fig. 1e, f). Crystal structures show that  $\phi X(V/P)X\phi$  motifs adopt a linear unfolded conformation to fit into the cleft of CSD dimers<sup>12</sup>. It is therefore plausible that a portion of the H2B  $\alpha$ 1-helix rearranges to resemble a short linear motif in order to bind the CSD. These experiments demonstrate that Swi6 interacts with the nucleosome core, in addition to the H3 tail, and that the CSD domain can specifically bind the H2B  $\alpha$ 1-helix (Fig. 1d).

We noticed several new H3–H3 and H4–H4 cross-links that arose in the Swi6-bound state (Extended Data Fig. 2g). These intra-histone cross-links are not within the standard distance captured by the cross-linker that was used. For example, the buried residues E97 and E105 of histone H3, the C $\alpha$  atoms of which are approximately 15 Å from the alpha carbon of K56, cross-link with K56 only in the presence of Swi6 (Fig. 1e, Extended Data Fig. 2h). Together with the possibility that CSD binding partially unfolds the H2B  $\alpha$ 1-helix, the new intra-histone cross-links suggest that Swi6 binding perturbs the canonical conformation of the histone octamer. Analogously, the previously observed interaction between mammalian HP1 proteins and the buried H3 $\alpha$ N helix region may also be indicative of a conformational change within the octamer<sup>10,11</sup>.

To test for the effect of Swi6 on nucleosome conformation more directly, we carried out hydrogen deuterium exchange mass

<sup>1</sup>Department of Pharmaceutical Chemistry, University of California San Francisco, San Francisco, CA, USA. <sup>2</sup>Department of Molecular Medicine, The Scripps Research Institute, Jupiter, FL, USA. <sup>3</sup>Program in Chemistry and Chemical Biology, University of California San Francisco, San Francisco, CA, USA. <sup>4</sup>Department of Biochemistry and Biophysics, University of California San Francisco, San Francisco, CA, USA. \*e-mail: jdgross@cgl.ucsf.edu; geeta.narlikar@ucsf.edu

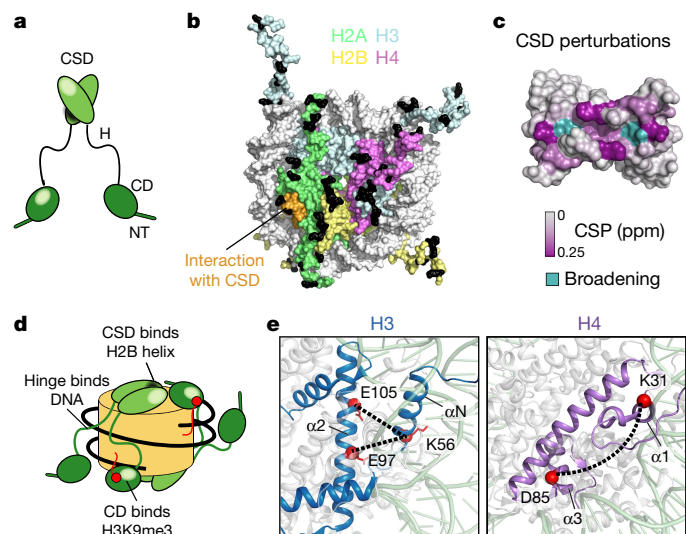


**Fig. 1 | Swi6 contacts histone octamer core and alters intra-histone cross-links.** **a**, Swi6 domain architecture. CD, chromodomain; H, hinge; NT, N-terminal region. **b**, Histone residues that cross-link to Swi6 are mapped in black on the nucleosome structure. Different histones are coloured as indicated. The H2B region interacting with the CSD is in orange. **c**, Swi6 CSD crystal structure is coloured by chemical shift perturbation (CSP; purple) and broadening beyond detection (teal) after the addition of H2B peptide (PDB code 1E0B). **d**, Model for engagement of Swi6 with nucleosomes. **e**, Swi6 binding remodels histone–histone contacts. Examples of residues found cross-linked only after Swi6 binding are represented as red spheres. Histones H3 and H4 are coloured in blue and purple, respectively.

spectrometry (HDX-MS) as a function of time on H3K9me3 mononucleosomes alone or in complex with saturating concentrations of Swi6 (Extended Data Fig. 3). This method measures the exchange of backbone amide hydrogens with solvent deuterium, and reports on protein backbone conformation, dynamics and solvent accessibility<sup>13</sup>.

Given the role of Swi6 in compaction of chromatin, the simplest expectation was that Swi6 would reduce solvent accessibility of mononucleosomes. Therefore, we expected decreased deuterium uptake after Swi6 binding, which is also a typical consequence of protein–protein interactions<sup>13</sup>. Instead, Swi6 binding resulted in a robust and widespread increase of deuterium incorporation throughout the histone octamer (Fig. 2a–c, Extended Data Fig. 3b, c). Notably, the H3 and H4 regions showing the highest degree of deuterium incorporation after Swi6 binding are buried within histone–histone and histone–DNA interfaces in the canonical nucleosome structure, which suggests partial unfolding of histone helices (Fig. 2d, e). These observations indicate that Swi6 binding causes a conformational change in the nucleosome that results in a widespread increase in the solvent accessibility of buried histone residues.

To characterize the effect of Swi6 on nucleosomes further, we used the orthogonal method of methyl-TROSY NMR spectroscopy, which allows studies of macromolecular assemblies as large as the proteasome and nucleosome<sup>14,15</sup>. In contrast to HDX-MS, this approach allows residue-level resolution, assessment of changes in magnetic environment due to binding or conformational changes and determination of the timescale of side-chain dynamics. H3 and H2B histones were labelled with <sup>13</sup>C on the methyl groups of isoleucine, leucine and valine (ILV) in an otherwise deuterated environment.

Binding of Swi6 to the nucleosome induced shifts and broadening of select resonances (Fig. 3a, b). Because Swi6 is deuterated, its binding affinity for the nucleosome is tight (dissociation constant ( $K_d$ ) < 100 nM), and nearly all of the ILV residues that undergo resonance broadening are buried, we interpret differential resonance

broadening as intramolecular conformational dynamics on the millisecond–microsecond timescale in the histone octamer core induced by Swi6 (Fig. 3c, d, Extended Data Fig. 4, Supplementary Table 1 for  $K_d$  values). Importantly, the changes in side-chain dynamics detected by NMR are consistent with the changes in backbone solvent accessibility detected by HDX-MS and the changes in intra-histone cross-links (Extended Data Fig. 5a, b). For example, H3 residues I51 and I62, which are strongly affected by Swi6 based on methyl-TROSY NMR, are in the histone regions that display higher deuterium uptake. The NMR results also rule out that disassembly of the nucleosome contributes to the HDX-MS data, because the cross-peaks of free histones fall in a different chemical shift region than what we observe<sup>15</sup>. Analogous millisecond–microsecond dynamics within the histone core were not observed in previous methyl-TROSY studies using a linker histone, which also enables chromatin compaction, suggesting that our observations reflect a Swi6-specific effect<sup>16</sup>.

On the basis of the results above, we propose that Swi6 loosens histone–histone and histone–DNA interactions through simultaneous engagement of the H3K9me3 mark by the chromodomain, the nucleosomal DNA by the hinge and the H2B  $\alpha$ 1 helix by the CSD dimer, allowing the buried histone residues to breathe and become solvent exposed (Fig. 1d, Extended Data Fig. 5c).

To test whether conformational changes inside the octamer are important for the assembly of Swi6 on nucleosomes, disulfide linkages that lock the octamer into its ground state conformation were employed<sup>15,17</sup>. If conformational rearrangements within the octamer core are energetically coupled to Swi6 binding, then constraining these rearrangements is predicted to reduce Swi6 binding affinity (Extended Data Fig. 5d, e). We introduced cysteine residues at H3-I62 and H4-A33 to lock this buried H3–H4 interface that showed major perturbations by NMR, HDX-MS and XLMS (Fig. 4a, Extended Data Fig. 5a). We generated nucleosomes with enzymatically methylated H3K9 and nearly 90% disulfide-linked histones (Extended Data Figs. 6a, 7). The disulfide cross-link reduces Swi6 affinity for H3K9me3 methylated nucleosomes by approximately fivefold, whereas it does not substantially affect binding to unmethylated nucleosomes (Extended Data Fig. 6b, c, Supplementary Table 1). Similar results were obtained with another set of disulfide linkages (Extended Data Fig. 6d–h, Supplementary Table 1). These results indicate that Swi6 binding and octamer distortion are coupled in the context of specific H3K9me3-recognition.

Notably, the binding of ZMET2, a plant DNA methyl-transferase that also binds H3K9me chromatin and bridges nucleosomes, is minimally affected by conformationally constrained nucleosomes<sup>18</sup> (Extended Data Fig. 6i). We conclude that nucleosome core distortion is not a general property of H3K9me binding proteins and that the ability of Swi6 to deform the octamer core relies on its specific interactions with the nucleosomal template.

The marked increase in conformational dynamics observed within single nucleosomes raised the possibility that these dynamics have a role in the compaction of chromatin by Swi6. We addressed this possibility using a classic *in vitro* method that monitors inter-array self-association via pelleting<sup>19</sup> (Extended Data Fig. 8a). We assembled 12 nucleosome-arrays containing the H3I62C–H4A33C cysteine pair. As observed previously for human HP1 proteins, we found that Swi6 pellets H3K9me3 nucleosome arrays in a dose-dependent manner when the dynamics at the H3–H4 interface are not restrained<sup>19</sup> (Fig. 4b). The concentration of Swi6 required to pellet 50% of the arrays (C50%) is approximately twofold greater for unmethylated versus methylated chromatin (Fig. 4b, Extended Data Fig. 8b). Moreover, the different shapes of the concentration dependencies suggest that the effect of Swi6 is less cooperative in the absence of H3K9me.

Notably, when observed under a microscope, the Swi6–nucleosome array pellets appear as phase-separated condensates (Fig. 4c and Extended Data Fig. 8c). Swi6 and nucleosome arrays formed these condensates under physiological conditions, whereas Swi6 and

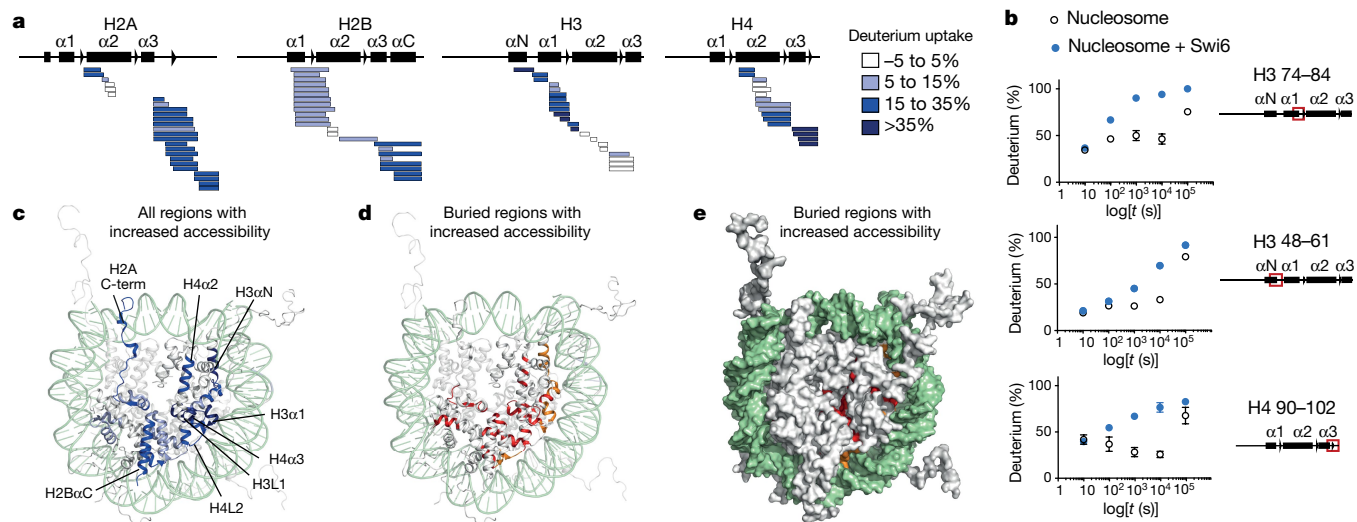


**Fig. 2 | Swi6 binding increases solvent accessibility of buried histone residues.** **a**, Differential HDX-MS of individual histones within Swi6-bound versus free nucleosomes from a single time point ( $10^4$  s; all time points in Extended Data Fig. 3b). Each horizontal bar represents an individual peptide. Peptides are placed beneath schematic of secondary structure elements. Colour map represents the percentage increase in deuterium uptake observed upon Swi6 binding. The percentage increase values are derived from several peptides obtained from one of two independent experiments with similar results. **b**, Kinetics of deuterium uptake of example histone peptides (residue

numbers indicated) over time ( $t$ ). Data are mean and s.d. of several peptides obtained from one of two independent experiments with similar results. Error bars not shown for points when shorter than the height of the symbol. **c**, Histones in nucleosome structure (PDB code 1KX5) coloured according to the percentage of deprotection in **a**. For clarity, only one copy of the histones is coloured. DNA is in light green. **d**, Histone-buried regions showing increase in deuterium uptake after Swi6 binding are highlighted. Residues proximal to DNA and histones are in orange and red, respectively. **e**, Histone regions in **d** shown in space-fill representation.

mononucleosomes, Swi6 alone, or arrays alone did not (Extended Data Fig. 8d, e). Similar to HP1 $\alpha$ , Swi6 can also form droplets in the presence of DNA alone<sup>5</sup> (Extended Data Fig. 8f). However, compared with arrays, a higher Swi6 concentration is required to form droplets with DNA alone. These data suggest that the multivalency provided by the nucleosome arrays as well as the specific Swi6–histone contacts are important to regulate phase separation driven by Swi6.

Further tests revealed that the Swi6-array condensates are liquid-like because they are reversible, can undergo fusion and are capable of exchanging contents<sup>20</sup> (Extended Data Fig. 9a–d). In addition, we observed a higher nucleosome concentration within the phase-separated condensate (Extended Data Fig. 9c, e). These results provide direct experimental evidence that Swi6 compacts chromatin into liquid condensates.

Disulfide-linkage of the H3–H4 interface substantially impairs the ability of Swi6 to pellet H3K9me3 nucleosome arrays into phase-separated droplets (Fig. 4b, c). Such impairment is not observed with unmethylated arrays (Extended Data Fig. 8b, c). Furthermore, neither ZMET2 nor a general protein denaturant can promote phase separation of arrays under matched conditions (Extended Data Fig. 8g, h). These results indicate that phase separation of chromatin relies on the types of histone core dynamics promoted by Swi6 in the presence of the H3K9me3 mark. Notably, the array experiments were performed using saturating Swi6 concentrations, indicating that, beyond enhancing Swi6 binding, octamer dynamics also promote inter-nucleosomal interactions (Supplementary Table 1, Methods). This conclusion was further validated by the observation that octamer dynamics are also required for chromatin sedimentation driven by Mg<sup>2+</sup> (Extended Data Fig. 8i). Notably, at 2 and 3 mM Mg<sup>2+</sup>, chromatin arrays form spherical droplets, raising the possibility that Mg<sup>2+</sup>-driven compaction can also be coupled to phase separation (Extended Data Fig. 8j). This finding is consistent with previous *in vitro* studies that show a lack of a defined structure in arrays that were cross-linked after Mg<sup>2+</sup>-dependent sedimentation<sup>21</sup>. On the basis of these results, we conclude that the dynamic exposure of buried histone core residues promotes compaction of

chromatin and phase separation, and that HP1 proteins play an active part in promoting such exposure.

Previous work has underscored the dynamic nature of HP1-mediated heterochromatin foci in cells<sup>6,22–24</sup>. This behaviour may be explained by the liquid-like properties that we observe for Swi6–chromatin droplets. To probe how *in vitro* Swi6–chromatin phase separation relates to *in vivo* heterochromatin organization, we used two Swi6 mutations that impair Swi6 oligomerization and gene silencing: the dimerX mutation, which inhibits dimer formation by the CSD, and the loopX mutation, which reduces higher order oligomerization<sup>4,25</sup> (Fig. 4d). Compared with wild-type Swi6, binding of both loopX and dimerX to mononucleosomes is minimally affected by restraining histone dynamics, which suggests that these mutants are defective in promoting nucleosome distortion (Extended Data Fig. 10a, b). Furthermore, the dimerX mutant fails to form phase-separated condensates with nucleosome arrays, even under saturating conditions for nucleosome binding (Fig. 4d, Extended Data Fig. 10c). This finding directly correlates with previous *in vivo* observations that Swi6 heterochromatin foci are disrupted by mutating the CSD<sup>25</sup>.

By contrast, the loopX mutant does not inhibit array phase separation, but forms larger droplets than wild-type Swi6 over time. Notably, these droplets show greater wetting behaviour than the droplets with wild-type Swi6, which suggests a lower surface tension and reduced stability of the system<sup>20</sup> (Fig. 4d, Extended Data Fig. 10c, d). The lower stability is consistent with the defective oligomerization of the loopX mutant<sup>4</sup>. Correspondingly, *in vivo*, we observed that the loopX mutation results in fewer and more diffuse Swi6 foci (Fig. 4e, Extended Data Fig. 10e). We conclude that the formation of Swi6–heterochromatin condensates relies on the ability of Swi6 to oligomerize and promote octamer distortion. Furthermore, changes in the intrinsic material properties of the Swi6–chromatin condensates *in vitro* correlate with changes in heterochromatin foci and gene silencing *in vivo*.

HP1 molecules have been shown to promote compaction of chromatin by bridging across nucleosomes as dimers or oligomers<sup>3,26</sup>. In addition, intrinsic chromatin compaction has been shown to involve

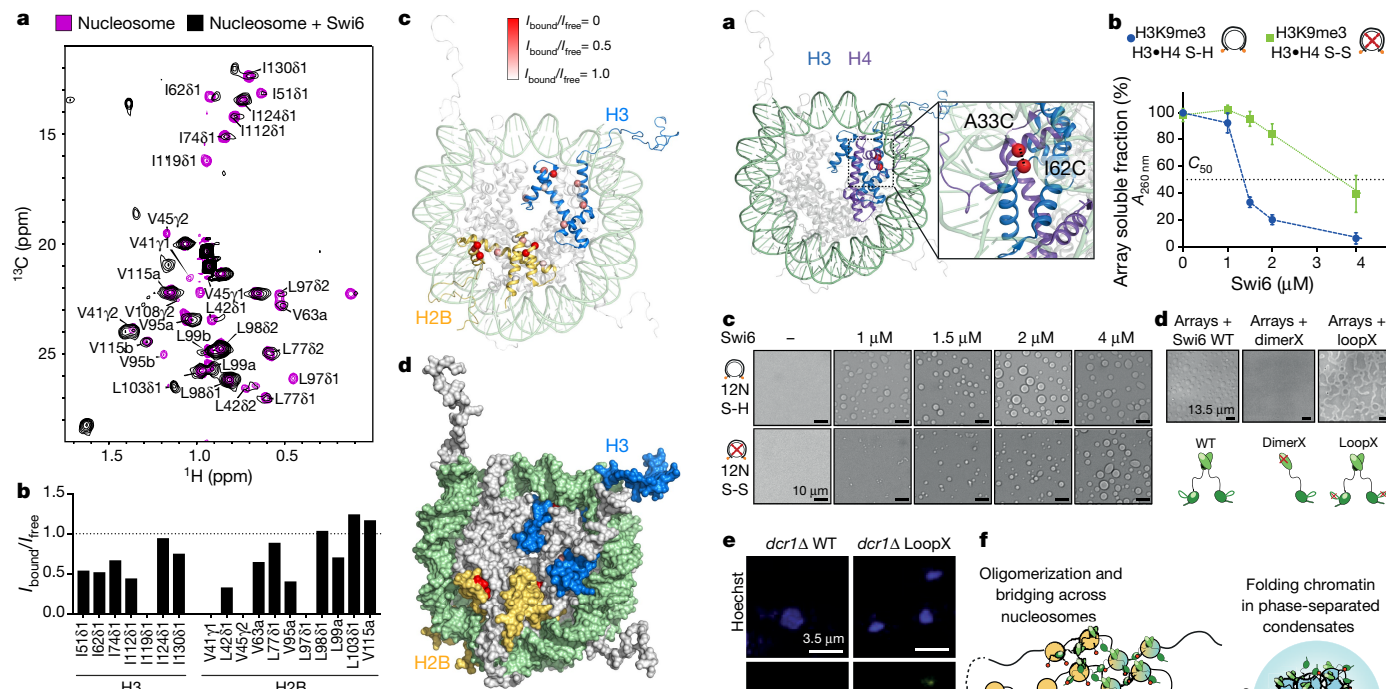


**Fig. 3 | Swi6 binding increases protein dynamics within octamer core.**

**a**, Methyl-TROSY spectra of Ile-methyl-labelled H3 and Leu/Val-methyl-labelled H2B in nucleosome alone (purple), and bound to Swi6 (black). Three resonances in H2B are not assigned as they correspond to residues V15, V38 and V66 present only in *Xenopus* H2B. Some resonances are largely unaffected (I124, L98, L99, V115 and two not assigned), whereas others are broadened and a few new resonances appear in the presence of Swi6. **b**, Peak volumes of H3 and H2B residues in the nucleosome–Swi6 complex ( $I_{\text{bound}}$ ) relative to those in the nucleosome alone ( $I_{\text{free}}$ ). Spectra were normalized using volumes of their respective L98 and two non-assigned peaks, which do not show broadening upon Swi6 binding. Only unambiguously assigned peaks are included in the quantification. Cross-peaks that disappear are taken to have an  $I_{\text{bound}}$  value of zero. **c**,  $\alpha$  of Ile residues in H3 and Leu or Val residues in H2B shown as red spheres in the nucleosome structure (PDB code 1KX5). Colour intensity of spheres represents extent of broadening determined by  $I_{\text{bound}}/I_{\text{free}}$ . **d**, Surface representation of nucleosome in **c**. Experiments were performed twice to optimize conditions; data from one experiment are reported.

interactions made by histone tails with nearby nucleosomes<sup>27</sup>. Our work uncovers another fundamental driver of chromatin compaction, namely the structural plasticity of the octamer core. We find that Swi6 leverages this plasticity to increase intrinsic histone core dynamics and accessibility by engaging the nucleosome core. The transient exposure of buried histone core residues can enable these residues to participate in weak multivalent interactions between nucleosomes, promoting formation of phase-separated liquid condensates<sup>20</sup>. We therefore propose that nucleosome disorganization by Swi6 together with the multivalency provided by Swi6 oligomerization drives the compaction of chromatin into phase-separated liquid droplets. This mechanism ultimately results in a less accessible chromatin state, consistent with the reduced histone turnover observed in *S. pombe* heterochromatin<sup>28</sup>.

Our model suggests mechanisms for how HP1 ligands can regulate the phase separation of heterochromatin: for example, by competing with the histone core for interaction with the CSD. Furthermore, functional differences among HP1 orthologues and paralogues can arise from differences in their ability to bind and reshape nucleosomes. For example, the different specificities of mammalian HP1 and Swi6 CSDs for histone and non-histone ligands may result in different ways of deforming the nucleosome core and thereby different mechanisms for fine-tuning heterochromatin phase separation<sup>7</sup>.

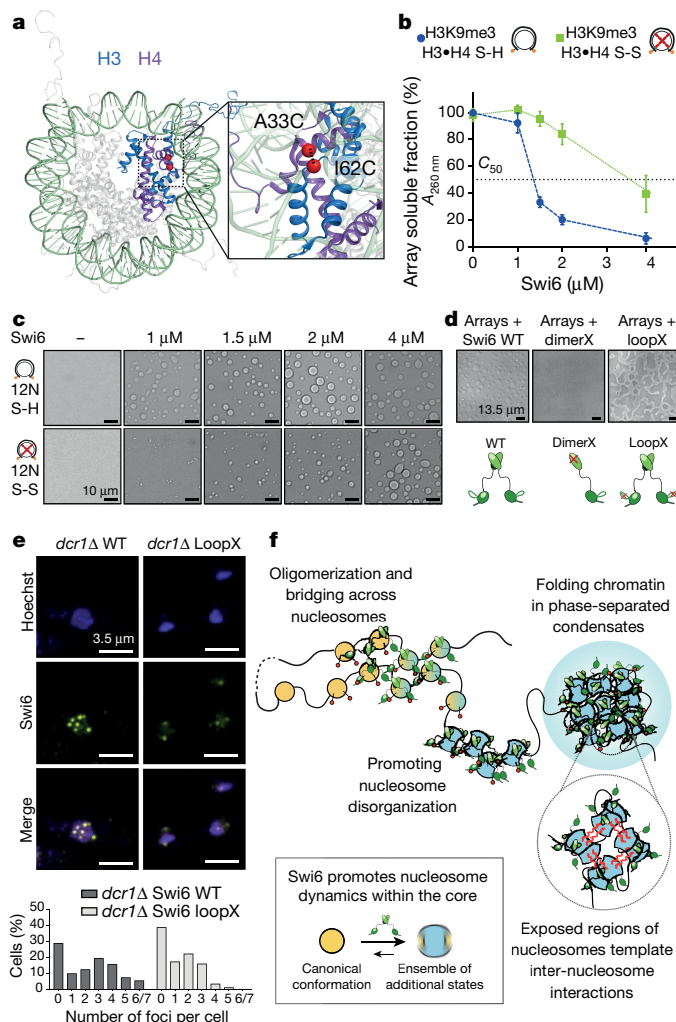


**Fig. 4 | Octamer dynamics promote Swi6-mediated compaction of chromatin and phase separation.**

**a**, Cysteine residues (red) introduced in H3 and H4 used for disulfide cross-links. **b**, Array self-association assays using nucleosome arrays containing H3K9me3•H4 S-S (oxidized, green) and H3K9me3•H4 S-H (reduced, blue) octamers as a function of increasing concentrations of Swi6. Dotted line represents  $C_{50}$ , the Swi6 concentration at which 50% of arrays sediment. Measurements entailed at least three independent experiments and error bars reflect s.d. **c**, Bright-field representative images of the Swi6-array mixtures analysed in **b**, showing phase-separated droplets. **d**, DimerX mutation abrogates Swi6-array droplet formation. LoopX-array droplets show higher wetting properties as seen by flatter morphology. Cartoons of respective Swi6 proteins are shown. Red crosses indicate mutation location. WT, wild type. Images in **c** and **d** are representative of at least three independent experiments. **e**, Compared with wild-type *S. pombe* cells, loopX cells show a reduced number of foci per cell and more diffuse nuclear staining. Top, representative images of wild-type or loopX mutant Swi6 cells. Bottom, quantification of Swi6 foci in wild-type and loopX mutant cells. Experiments were repeated independently at least three times and more than 250 cells per condition were analysed. **f**, Model for Swi6–heterochromatin. Oligomerization of Swi6 (green) on H3K9me3-marked (red spheres) nucleosomes loosens histone–DNA and histone–histone contacts, increasing dynamics within the octamer core. Nucleosomes can then access larger ensemble of dynamically interconverting conformational states, increasing opportunities for transient weak multivalent interactions with other nucleosomes, including histone tails. Such interactions and nucleosome bridging by Swi6 enable the compaction of chromatin into liquid droplets. Black box shows that nucleosomes in solution can sample an ensemble of conformational states, of which the canonical conformation (orange) observed in the crystal structure is the most populated. Swi6 increases intrinsic histone core dynamics and accessibility. As a result, this increases the proportion of alternative conformational states of the nucleosome (blue).

Our work also raises the possibility that histone modifications and histone variants modify chromatin compaction by directly affecting the conformational plasticity of the histone octamer.

More generally, the phase separation- and octamer deformation-based mechanism for compaction of chromatin proposed here can explain how the genome can be functionally organized without invoking structures such as the 30-nm fibre<sup>29</sup>. Indeed, consistent with such a possibility, recent reports suggest that nucleosomes in mitotic chromatin adopt non-canonical conformations<sup>30</sup>. Future studies will uncover how broadly octamer plasticity and phase separation regulate chromatin organization.

## Online content

Any methods, additional references, Nature Research reporting summaries, source data, extended data, supplementary information, acknowledgements, peer review information; details of author contributions and competing interests; and statements of data and code availability are available at <https://doi.org/10.1038/s41586-019-1669-2>.

- Stephens, A. D. et al. Chromatin histone modifications and rigidity affect nuclear morphology independent of lamins. *Mol. Biol. Cell* **29**, 220–233 (2018).
- Allshire, R. C. & Madhani, H. D. Ten principles of heterochromatin formation and function. *Nat. Rev. Mol. Cell Biol.* **19**, 229–244 (2018).
- Canzio, D. et al. Chromodomain-mediated oligomerization of HP1 suggests a nucleosome-bridging mechanism for heterochromatin assembly. *Mol. Cell* **41**, 67–81 (2011).
- Canzio, D. et al. A conformational switch in HP1 releases auto-inhibition to drive heterochromatin assembly. *Nature* **496**, 377–381 (2013).
- Larson, A. G. et al. Liquid droplet formation by HP1α suggests a role for phase separation in heterochromatin. *Nature* **547**, 236–240 (2017).
- Strom, A. R. et al. Phase separation drives heterochromatin domain formation. *Nature* **547**, 241–245 (2017).
- Eissenberg, J. C. & Elgin, S. C. R. HP1α: a structural chromosomal protein regulating transcription. *Trends Genet.* **30**, 103–110 (2014).
- Smothers, J. F. & Henikoff, S. The HP1 chromo shadow domain binds a consensus peptide pentamer. *Curr. Biol.* **10**, 27–30 (2000).
- Isaac, R. S. et al. Biochemical basis for distinct roles of the heterochromatin proteins Swi6 and Chp2. *J. Mol. Biol.* **429**, 3666–3677 (2017).
- Dawson, M. A. et al. JAK2 phosphorylates histone H3Y41 and excludes HP1α from chromatin. *Nature* **461**, 819–822 (2009).
- Lavigne, M. et al. Interaction of HP1 and Brg1/Brm with the globular domain of histone H3 is required for HP1-mediated repression. *PLoS Genet.* **5**, e1000769 (2009).
- Liu, Y. et al. Peptide recognition by HP1 chromoshadow domains revisited: plasticity in the pseudosymmetric histone binding site of human HP1. *J. Biol. Chem.* **292**, 5655–5664 (2017).
- Hoofnagle, A. N., Resing, K. A. & Ahn, N. G. Protein analysis by hydrogen exchange mass spectrometry. *Annu. Rev. Biophys. Biomol. Struct.* **32**, 1–25 (2003).
- Rosenzweig, R. & Kay, L. E. Bringing dynamic molecular machines into focus by methyl-TROSY NMR. *Annu. Rev. Biochem.* **83**, 291–315 (2014).
- Sinha, K. K., Gross, J. D. & Narlikar, G. J. Distortion of histone octamer core promotes nucleosome mobilization by a chromatin remodeler. *Science* **355**, eaaa3761 (2017).
- Zhou, B.-R. et al. Structural insights into the histone H1-nucleosome complex. *Proc. Natl Acad. Sci. USA* **110**, 19390–19395 (2013).
- Luger, K., Mäder, A. W., Richmond, R. K., Sargent, D. F. & Richmond, T. J. Crystal structure of the nucleosome core particle at 2.8 Å resolution. *Nature* **389**, 251–260 (1997).
- Stoddard, C. I. et al. A nucleosome bridging mechanism for activation of a maintenance DNA methyltransferase. *Mol. Cell* **73**, 73–83.e6 (2019).
- Azzaz, A. M. et al. Human heterochromatin protein 1α promotes nucleosome associations that drive chromatin condensation. *J. Biol. Chem.* **289**, 6850–6861 (2014).
- Alberti, S., Gladfelter, A. & Mittag, T. Considerations and challenges in studying liquid-liquid phase separation and biomolecular condensates. *Cell* **176**, 419–434 (2019).
- Maeshima, K. et al. Nucleosomal arrays self-assemble into supramolecular globular structures lacking 30-nm fibers. *EMBO J.* **35**, 1115–1132 (2016).
- Cheutin, T., Gorski, S. A., May, K. M., Singh, P. B. & Misteli, T. *In vivo* dynamics of Swi6 in yeast: evidence for a stochastic model of heterochromatin. *Mol. Cell. Biol.* **24**, 3157–3167 (2004).
- Cheutin, T. et al. Maintenance of stable heterochromatin domains by dynamic HP1 binding. *Science* **299**, 721–725 (2003).
- Festenstein, R. et al. Modulation of heterochromatin protein 1 dynamics in primary mammalian cells. *Science* **299**, 719–721 (2003).
- Haldar, S., Saini, A., Nanda, J. S., Saini, S. & Singh, J. Role of Swi6/HP1 self-association-mediated recruitment of Ctr4/Suv39 in establishment and maintenance of heterochromatin in fission yeast. *J. Biol. Chem.* **286**, 9308–9320 (2011).
- Kilic, S., Bachmann, A. L., Bryan, L. C. & Fierz, B. Multivalency governs HP1α association dynamics with the silent chromatin state. *Nat. Commun.* **6**, 7313 (2015).
- Kalashnikova, A. A., Porter-Goff, M. E., Muthurajan, U. M., Luger, K. & Hansen, J. C. The role of the nucleosome acidic patch in modulating higher order chromatin structure. *J. R. Soc. Interface* **10**, 20121022–20121022 (2013).
- Aygün, O., Mehta, S. & Grewal, S. I. S. HDAC-mediated suppression of histone turnover promotes epigenetic stability of heterochromatin. *Nat. Struct. Mol. Biol.* **20**, 547–554 (2013).
- Fussner, E., Ching, R. W. & Bazett-Jones, D. P. Living without 30nm chromatin fibers. *Trends Biochem. Sci.* **36**, 1–6 (2011).
- Cai, S. et al. Cryo-ET reveals the macromolecular reorganization of *S. pombe* mitotic chromosomes *in vivo*. *Proc. Natl Acad. Sci. USA* **115**, 10977–10982 (2018).

**Publisher's note** Springer Nature remains neutral with regard to jurisdictional claims in published maps and institutional affiliations.

© The Author(s), under exclusive licence to Springer Nature Limited 2019

## Methods

### Data reporting

No statistical methods were used to predetermine sample size. The experiments were not randomized, and investigators were not blinded to allocation during experiments and outcome assessment.

### Protein expression, purification and isotope labelling

All the histones were expressed and purified from *Escherichia coli* following published protocols<sup>31</sup> with some modifications for the isotopically labelled histones. For expression of deuterated histones, M9 minimal media was made in deuterium oxide (D<sub>2</sub>O, Cambridge Isotope Laboratories). The media contained D-glucose-1,2,3,4,5,6,6-*d*<sub>7</sub> (Cambridge Isotope Laboratories or Sigma-Aldrich) as the sole carbon source. For labelling the histones at ILV residues, <sup>13</sup>CH<sub>3</sub>-methyl group  $\alpha$ -ketoisobutyrate and  $\alpha$ -ketoisovalerate (Cambridge Isotope Laboratories) were added to the M9 media as precursors<sup>32</sup>. To optimize coverage and spectral resolution, nucleosomes were labelled with isoleucine on histone H3, whereas histone H2B was labelled with leucine and valine. This labelling scheme maximizes the distribution of methyl probes across the nucleosome core and minimizes dephasing due to inter methyl-group dipolar interactions<sup>33</sup>. Deuteration and ILV labelling of the histones were confirmed by mass spectrometry. All the mutant versions of the histones were made by quick-change site-directed mutagenesis or the Gibson Assembly method. All mutations were confirmed by sequencing the plasmids.

Methyl lysine analogues containing H3 histones at position 9 (H3K<sub>9</sub>me3) were prepared as described previously<sup>34</sup>.

N-terminally 6 $\times$ -His tagged Swi6 was purified from an *E. coli* as previously described<sup>3</sup>. In brief, Swi6 was affinity purified with cobalt beads followed by TEV protease treatment to cleave the N-terminal 6 $\times$ -His tag. After TEV cleavage, it was subjected to HiTrap Q HP column (GE Healthcare) and Superdex 200HR 10/300 column (GE Healthcare). Swi6 is stored in 25 mM HEPES, pH 7.5, 150 mM KCl, 1 mM dithiothreitol (DTT) and 10% glycerol. For expression of deuterated Swi6, M9 minimal media was made in deuterium oxide (D<sub>2</sub>O, Cambridge Isotope Laboratories) with D-glucose-1,2,3,4,5,6,6-*d*<sub>7</sub> (Cambridge Isotope Laboratories) as the only carbon source.

<sup>15</sup>N-labelled CSD was expressed in M9 minimal media containing <sup>15</sup>N-ammonium chloride as the sole nitrogen source. The CSD was purified as previously described<sup>9</sup>.

The GST-Dim5 plasmid was provided by I. Suetake. GST-Dim5 was expressed in Rosetta cells in presence of 10  $\mu$ M ZnSO<sub>4</sub> as previously described<sup>35</sup>. Cells were lysed in 20 mM Tris, pH 9.6, 500 mM NaCl, 0.05% NP40, 1 mM DTT and protease inhibitor EDTA-free. The protein is first purified on a GSTRap FF column (GE Healthcare), then on HiTrap Q HP column. Purified Dim5 is stored in 20 mM Tris, pH 9.6, 150 mM NaCl, 1 mM DTT and 5% glycerol.

### H3K9 enzymatic methylation

Dim5 was dialysed in the methylation buffer: 100 mM Tris-Cl, pH 9.6, 20  $\mu$ M ZnSO<sub>4</sub>, 2 mM  $\beta$ -mercaptoethanol, 10 mM KCl, 10 mM MgCl<sub>2</sub> plus 80 mM NaCl. Histone H3 mutants C110A and I62C were resuspended in methylation buffer at 0.1 mg ml<sup>-1</sup>. The reaction condition was as previously described<sup>36</sup> and carried out at room temperature for 3 h with 1:2 molar ratio of histone:Dim5 in the presence of 50  $\mu$ M S-adenosylmethionine (SAM; NEB). The reaction pH is adjusted to 9.8 after the addition of SAM. The reaction is then mixed with four volumes of 9 M deionized urea, and reagents added to reach 200 mM NaCl, 20 mM NaAc, pH 5.2, 1 mM EDTA, 5 mM  $\beta$ -mercaptoethanol as final concentration. The sample pH is adjusted to 5.2 before loading it on a HiTrap SP HP cation exchange chromatography column (GE Healthcare), and eluted with a salt gradient. The histone is collected, dialysed in H<sub>2</sub>O with 5 mM  $\beta$ -mercaptoethanol and diluted ten times with 0.1% formic acid for mass spectrometry analysis.

Methylation was followed using electron transfer dissociation (ETD)-based liquid chromatography–tandem mass spectrometry (LC–MS/MS) of the intact histone. The protein was separated over a 15 cm  $\times$  75  $\mu$ m ID PepMap C18 column (Thermo) using a NanoAcquity UPLC system (Waters) running a gradient from 10–75% B (acetonitrile plus 0.1% formic acid) at 300 nl min<sup>-1</sup> over 40 min. Analysis was performed by an online Orbitrap Fusion Lumos (Thermo) mass spectrometer. Precursor ions were measured at 120,000 resolution in the Orbitrap (automatic gain control (AGC):  $1 \times 10^6$ ). Ions that were 15–22<sup>+</sup> charged with intensity greater than  $1 \times 10^6$  were isolated in the quadrupole (1.8 *m/z* isolation window) and fragmented by ETD for 4 ms. Product ions were measured in the Orbitrap at 30,000 resolution (AGC:  $9 \times 10^5$ , maximum injection time: 250 ms, 3 microscans).

Precursor ion spectra were deisotoped using Xtract (Thermo). The deconvoluted M + H of the untreated histone (15,220.442) was consistent with the expected mass of the H3(I62C) mutant (15,220.554) to 7.4 ppm and was about 11% oxidized on methionine. Enzymatic methylation produced a pattern of deconvoluted M + H signals spaced 14 Da apart, although some of these signals were off by  $\pm 1$  Da owing to challenging monoisotopic peak detection. These were confirmed as methylations by bottom-up proteomic analysis of Lys-C-digested sample. The methylated sample had no detectable unmethylated, monomethylated or dimethylated species. All of the ions signals for which the ETD spectra were available showed 100% trimethylation at H3K9 based on their c-ions. Additional methylations could be localized to H3K18 and K3K14 (Extended Data Fig. 7).

### Mononucleosome assembly

Histone octamer was assembled from purified histones by salt dialysis as previously described<sup>37</sup>. The 601 positioning sequence (147 bp) DNA fragment was made using restriction enzyme digestion of a plasmid carrying multiple copies of 601 DNA fragment as described previously<sup>31</sup>. Fluorescence DNA was generated by PCR amplification using a primer 5'-labelled with 5,6 carboxy-fluorescein (IDT) followed by gel purification<sup>4</sup>. Nucleosomes were assembled using published gradient dialysis based protocols<sup>31</sup>. The purification of the nucleosomes was carried out on a 10–30% glycerol gradient. For NMR experiments, the glycerol gradient step was replaced by gel filtration purification with a Superdex-200 column.

Disulfide cross-linked nucleosomes were made using histone Cys variants, see Supplementary Tables 1 and 2. To maximize the likelihood of disulfide bridge formation, the cysteine pairs were selected so as to have an interatomic distance  $\leq 5$  Å between the sulfur atoms facing each other, to have side chains pointing towards each other in the structure and to form bonds in Coot (<https://www2.mrc-lmb.cam.ac.uk/personal/pemsley/coot/>). All the cysteine variant histone proteins were purified in the presence of excess DTT during all the steps of protein purification. To purify the cysteine variants, only the gel filtration step was carried out, as previously described<sup>15</sup>. For reduced nucleosome, the assembly and subsequent purification were carried out in the presence of 3 mM tris(2-carboxyethyl) phosphine) (TCEP) in all the buffers. For disulfide-linked nucleosome formation, the octamer was subjected to oxidizing conditions. First, the octamer sample was diluted to a final octamer concentration of 0.5 mg ml<sup>-1</sup> to minimize the formation of any intermolecular cross-links. Then it was subjected to three consecutive dialysis in refolding buffer (pH 8.5) in the absence of any reducing agent as previously described<sup>15</sup>. Finally, the solution containing octamers was mixed 4:1 with a solution containing 250 mM Tris-Cl, pH 9, 2 M NaCl, 2.5 mM oxidized glutathione, 2.5 mM reduced glutathione and incubated 12 h at room temperature as previously described<sup>38</sup>. The sample was then dialysed in refolding buffer with no reducing agent, before proceeding to nucleosome assembly. The cross-linking efficiency was confirmed by running the sample on a 15% non-reducing SDS gel.

## 12 nucleosome-array assembly

DNA was generated by restriction enzyme digestion of a plasmid containing 12 consecutive 601s spaced by 20 bp, followed by gel purification. The reconstitution of nucleosome arrays followed the protocols described with some modifications<sup>39</sup>. Histone octamers are combined in equimolar amount with 12-mer DNA (12 repeats of the 601 DNA sequence separated by 20-bp linkers). Final dialysis against 10 mM TEK (10 mM KCl, 10 mM Tris, pH 7.5, 0.1 mM EDTA) was performed overnight. After assembly, arrays were usually used for experiments within 1–2 days after assembly. Because the 601 repeats in the 12-mer DNA sequence are separated by HpaI restriction enzyme sites, the quality of assembly was assessed by HpaI digestion followed by native gel. Over-assembly was avoided by ensuring that >95% of the digested fragments migrated as mononucleosomes rather than slower migrating species. We note that the quality of the arrays used in these studies had to be carefully controlled to avoid over-assembly of histone octamers, as we noticed that over-assembled arrays displayed aberrant and non-reproducible precipitation behaviour (Extended Data Fig. 8k).

## Chromatin self-association assay

Swi6-mediated array self-association assays were performed at 40 nM nucleosome arrays in 10 mM Tris, 0.1 mM EDTA, 75 mM KCl, pH 7.8. In brief, 5 µl of 2× array sample (80 nM) were incubated with 5 µl of 2× Swi6 solution for 20 min at 22 °C. Samples were centrifuged at 10,000g for 10 min at 22 °C, and the supernatants were transferred to a fresh tube. Five microliters of the supernatant was read at 260 nm. At least three technical and biological replicates were performed for each experiment. Mg<sup>2+</sup> self-association assays were performed in TE 0.1 (10 mM Tris pH 7.8, 0.1 mM EDTA).

## Liquid droplets microscopy

Microscopy of the droplets was done on a Leica Axiovert 200M microscope using a 20× air objective and on a Zeiss Axiovert 200M Fluorescence microscope. Samples were imaged on a 384-well plate, glass bottom, coated with Peg-silane (Laysan Bio). Image analysis was done in ImageJ.

## Fluorescence polarization binding measurement

Nucleosome polarization assays were conducted in buffer containing 0.02% NP-40, 150 mM KCl, 20 mM HEPES, pH 7.5, and 1 mM DTT at 22 °C. Each anisotropy sample contained a final nucleosome concentration of 5 nM and the Swi6 concentration was varied. The reaction was incubated 30 min at 22 °C and fluorescence polarization was measured on an Analyst HT (Molecular Devices). Data points from three independent Swi6 dilution curves were averaged and standard errors calculated. The following binding model was used to derive  $K_d$ :

$$Y = ((X^N \times FP_{\max}) + (K_d^N \times FP_{\min})) / (X^N + K_d^N)$$

in which  $Y$  is the fluorescence polarization signal observed;  $X$  is the Swi6 concentration;  $FP_{\min}$  is the fluorescence polarization signal for the probe alone;  $FP_{\max}$  is the fluorescence polarization signal at saturating protein concentration; and  $N$  is the Hill coefficient.

## Nucleosome NMR sample preparation and spectroscopy

The nucleosome storage buffer was exchanged with NMR buffer by dialysis. The NMR buffer was made in D<sub>2</sub>O and contained 70 mM NaPO<sub>4</sub> (pD 7.6), 10 mM deuterated DTT. The nucleosome concentration used was 50 µM. For the experiment involving the Swi6–nucleosome complex, Swi6 was buffer exchanged in the NMR buffer. Nucleosome and Swi6 were mixed in a 1:6 molar ratio to get four Swi6 molecules per nucleosome. The Swi6 concentration was saturating in the concentration regime used.

All the NMR spectra were acquired at 303 K on a Bruker 600 MHz spectrometer equipped with a Cryoprobe. Recorded spectra were processed using the NMRPipe software and displayed using SPARKY (<http://www.cgl.ucsf.edu/home/sparky/>)<sup>40</sup>. The assignments were transferred from published spectra of *Drosophila* nucleosome by inspection<sup>41</sup>. The two sets of spectra were remarkably similar owing to sequence conservation between *Drosophila* and *Xenopus* histones H3 and H2B (Extended Data Fig. 4a, b). A comparison of the chemical shift positions across *Drosophila* and *Xenopus* histone spectra suggested very small differences between the two, with the average  $\Delta\delta$  (ppm) being less than 0.05 (Extended Data 4a). Buffer and temperature were selected based on optimal conditions screened by fluorescence polarization.

The concentrations of Swi6–mononucleosome complexes used for the NMR experiments did not display detectable aggregation or phase separation as evaluated using two different metrics. First, analytical ultracentrifugation carried out at comparable concentrations of the complex did not detect higher-order species beyond four Swi6 molecules bound to a mononucleosome. Second, the NMR data did not show significant overall signal loss for up to around 60 h of measurement time. Precipitation or aggregation is expected to result in signal loss due to overall broadening of all the cross-peak signals.

## CSD NMR

Binding experiments were carried out with 80 µM <sup>15</sup>N-CSD and 160 µM H2B peptide (dissolved in H<sub>2</sub>O, pH adjusted to 7.8) in 150 mM KCl, 20 mM HEPES pH 7.8, 2 mM DTT. HSQC spectra were recorded at 298K on a Bruker Avance DRX500 spectrometer.

Chemical shift perturbations were calculated from the equation:

$$\sqrt{0.5((\delta H_{\text{bound}} - \delta H_{\text{free}})^2 + (0.2(\delta N_{\text{bound}} - \delta N_{\text{free}}))^2)}$$

in which the factor 0.2 is used as a scaling factor for nitrogen spectral width, and  $\delta H$  and  $\delta N$  are chemical shifts in the <sup>1</sup>H and <sup>15</sup>N dimensions, respectively.

## HDX-MS

Solution-phase amide HDX experiments were carried out with a fully automated system described previously with slight modifications<sup>42</sup>. Five microliters of apo-nucleosome or nucleosome-Swi6 complex (1:4) was mixed with 20 µl of D<sub>2</sub>O-containing HDX buffer (20 mM Hepes pH 7.5, 150 mM KCl, 10% glycerol, and 10 mM DTT) and incubated at 22 °C for a range of time points (0, 10, 10<sup>2</sup>, 10<sup>3</sup>, 10<sup>4</sup> or 10<sup>5</sup> s). Each HDX experiment was carried out in triplicate with a single preparation of each protein–ligand complex. Following on-exchange, unwanted forward or back exchange was minimized and the protein was denatured with a quench solution (5 M urea, 50 mM TCEP and 1% (v/v) TFA pH 2.5) at 1:1 ratio to protein. Samples were then passed through an in-house prepared immobilized pepsin column at 50 µl min<sup>-1</sup> (0.1% (v/v) TFA, 15 °C) and the resulting peptides were trapped on a C<sub>8</sub> trap column (Hypersil Gold, Thermo Fisher). The bound peptides were then gradient-eluted (5–50% CH<sub>3</sub>CN (w/v) and 0.3% w/v formic acid) across a 1 mm × 50 mm C<sub>18</sub> HPLC column (Hypersil Gold, Thermo Fisher) for 5 min at 4 °C. The eluted peptides were then analysed directly using a high resolution Orbitrap mass spectrometer (Q Exactive, Thermo Fisher). To identify peptides, MS/MS experiments were performed on Q Exactive Orbitrap mass spectrometer over a 70 min gradient. Product ion spectra were acquired in a data-dependent mode and the five most abundant ions were selected for the product ion analysis. The MS/MS\*.raw data files were converted to \*.mgf files and then submitted to Mascot (Matrix Science) for peptide identification. Peptides with a Mascot score of 20 or greater were included in the peptide set used for HDX detection. The MS/MS Mascot (Matrix Science) search was also performed against a decoy (reverse) sequence and false positives were ruled out. The MS/MS spectra of all the peptide ions from the Mascot search were further manually inspected and only the unique charged ions with the

highest Mascot score were used in estimating the sequence coverage. Peptic digestion of nucleosomes yielded approximately 70% sequence coverage of the histone core and minimal coverage on the histone tails. By observing overlapping peptic peptides we could unambiguously assign the HDX-MS data to the histones<sup>43</sup>. Percentage deuterium exchange values for peptide isotopic envelopes at each time point were calculated and processed using HDX Workbench<sup>44</sup>. The intensity weighted mean *m/z* centroid value of each peptide envelope was calculated and subsequently converted into a percentage of deuterium incorporation. This is accomplished by determining the observed averages of the undeuterated and using the conventional formula described elsewhere<sup>45</sup>. Corrections for back-exchange were made on the basis of an estimated 70% deuterium recovery and accounting for 80% final deuterium concentration in the sample (1:5 dilution in D<sub>2</sub>O HDX buffer). Deuterium uptake for each peptide is calculated for each of time points and the difference in percentage D values between the po-nucleosome and nucleosome–Swi6 samples is shown as a heat map with a colour code given at the bottom of the figure.

### Cross-linking mass spectrometry

Trimethyl lysine analogue H3K9 mononucleosomes (85 µg, 20 µM) either with or without Swi6 (80 µM) in buffer A (20 mM HEPES, 150 mM KCl and 2 mM DTT, pH 7.5) were reacted with 25 µM 1-ethyl-3-(3-dimethylaminopropyl)carbodiimide (EDC; added as 10× stock in buffer A) and 0.5 µM *N*-hydroxysulfosuccinimide (added as 15× stock in buffer A) for 60 min at 25 °C. The reactions were quenched by adding 50 mM Tris-base and 20 mM β-mercaptoethanol and incubating for 15 min at 25 °C. Samples were acetone precipitated and washed once with cold acetone. The pellet was resuspended in 8 M urea, 10 mM TCEP, 100 mM ammonium bicarbonate and heated at 56 °C for 20 min, followed by alkylation with 20 mM iodoacetamide for 45 min at room temperature. The sample was diluted sixfold with 100 mM ammonium bicarbonate and digested with 1:25 trypsin for 4 h at 37 °C followed by addition of a second aliquot of trypsin and overnight digestion.

Cross-linked peptides were desalted, fractionated by size-exclusion chromatography (SEC), and analysed by LC–MS as previously described<sup>46</sup>. In brief, trypsin digests were acidified to 0.2% TFA, desalted, and run over a Superdex Peptide PC 3.2/300 SEC column (GE Healthcare). SEC fractions eluting between 0.9 ml and 1.4 ml were dried and resuspended in 0.1% formic acid for LC–MS. Each fraction was separated over a 15 cm × 75 µm ID PepMap C18 column (Thermo) using a NanoAcquity UPLC system (Waters) and analysed by a Q-Exactive Plus mass spectrometer (Thermo). The top 10 most abundant, triply charged and higher precursor ions (measured at 70,000 resolution) were selected for HCD (NCE: 24.5) and measured at 17,500 resolution.

Peak lists were generated using Proteome Discoverer 1.4 (Thermo) and searched for cross-linked peptides with Protein Prospector 5.17.2 against a target database containing Swi6 from *S. pombe* plus the four core histone sequences from *Xenopus laevis* concatenated with a decoy database containing 10 randomized copies of each target sequence (total database size 60 sequences)<sup>47</sup>. Tri-methylation of histone H3 at K9 was treated as a constant modification as was loss of the initiator methionine and carbamidomethylation of cysteine. Methionine oxidation, peptide N-terminal glutamine to pyroglutamate formation, acetylation at the protein N terminus, and mis-annotation of the monoisotopic peak (1 Da neutral loss) were treated as variable modifications. EDC was designated as a heterobifunctional cross-linking reagent with specificity of aspartate, glutamate, and the protein C terminus on one side and lysine and the protein N terminus on the other with a bridge mass corresponding to loss of H<sub>2</sub>O. A mass modification range of 400–5,000 Da was specified on these residues and 85 product ion peaks from the peaklist were used in the search. Precursor and product ion tolerances were 10 and 25 ppm respectively.

Cross-linked spectral matches were classified using a support vector machine based scoring model as described previously<sup>46</sup>. Crosslinked

residue pairs were reported that had Score Difference >5, detoo (SVM) Score >0.1, peptide length >4, and number of spectral counts >= 1. The final residue-pair level false discovery rate was 0.5%. Crosslink spectral counts were assigned to residue-pairs and domain-pairs in a way that normalized for ambiguous site-localization as previously detailed<sup>46</sup>. Solvent accessible surface values were generated from surface calculation using UCSF Chimera and the nucleosome structure for PDB code 1KXF.

### Sedimentation velocity analytical ultracentrifugation

Sedimentation velocity experiments were conducted using an analytical ultra-centrifuge (Beckman Coulter) equipped with an absorption optical scanner. The binding reaction was set up such that (i) both nucleosome and Swi6 concentrations were above the  $K_{1/2}$  value measured by native gel and (ii) the Swi6 concentration was sufficient to titrate all the nucleosomes as assayed by native gel shift. Solution density ( $\rho$ ) and solution viscosity ( $\eta$ ) were calculated in SEDNTERP<sup>48</sup>. Data were analysed using the Sedfit software and plots were generated using GUSSE<sup>48,49</sup>. Experiments were performed with 200 nM dinucleosome and 10 µM Swi6, in 20 mM HEPES, pH 7.6, 150 mM KCl and 1 mM DTT at 24 °C, spinning at 36,000 rpm for 8 h. The continuous  $c(s)$  and  $c(s, bimodal fr)$  analysis was used to study the sedimentation properties and the molar mass of the dinucleosome and dinucleosome–Swi6 samples, respectively.

### *S. pombe* growth and immunostaining

Cells were grown to mid log phase, OD<sub>600nm</sub> = 0.2–0.4 per ml in supplemented YE medium. The culture was made 1.2 M with respect to sorbitol by adding an equal volume of 2.4 M sorbitol in PBS about 5 min before fixation. Cells were fixed for 30 min at 20 °C in 3.8% para-formaldehyde. Cells were washed in PEMS buffer and cell walls were digested by 1.0 mg ml<sup>-1</sup> zymolyase 100T for 70 min at 37 °C, lysed by 5 min incubation in PEMS containing 1% Triton X-100 and then washed three times in PEM buffer before incubation for 30 min in PEM buffer with 1% bovine serum albumin, 0.1% sodium azide and 100 mM lysine hydrochloride (PEMBAL) buffer. Rabbit Swi6 antibody was used for overnight incubation with cells in PEMBAL at 4 °C. Stained cells were washed three times in PEMBAL and then incubated with secondary antibody for 1h at room temperature. Staining with Hoechst was performed before mounting cells on slides. Microscopy was done on a Nikon Ti confocal microscope using a 100X objective. Image analysis was done in ImageJ. Cells were authenticated by immunostaining.

*S. pombe* strains used in this study are described previously<sup>4</sup>: PM0251: P(h+), ura4-DS/E, ade6-M210, leu1-32, imr1L(NcoI)::ura4, otr1R(Sph1)::ade6; DC27: PM0251, *swi6*Δ::KanMX::KanMX, *dcr1*Δ::NatMX; DC30: PM0251, *swi6*::KanMX::KanMX, *dcr1*Δ::NatMX; DC32: PM0251, *swi6* (R93A-K94A)::KanMX::KanMX, *dcr1*Δ::NatMX.

### Reporting summary

Further information on research design is available in the Nature Research Reporting Summary linked to this paper.

### Data availability

All relevant data that support the findings of this study are available within the paper and its Supplementary Information files. Annotated XLMS Spectra are available using MS-Viewer at: <http://msviewer.ucsf.edu/prospector/cgi-bin/msform.cgi?form=msviewer> using the search key: 9ojpmsdzk5. Any additional data are available from the corresponding author upon reasonable request.

31. Dyer, P. N. et al. Reconstitution of nucleosome core particles from recombinant histones and DNA. *Methods Enzymol.* **375**, 23–44 (2003).

32. Tugarinov, V., Kanelis, V. & Kay, L. E. Isotope labeling strategies for the study of high-molecular-weight proteins by solution NMR spectroscopy. *Nat. Protoc.* **1**, 749–754 (2006).

33. Hamel, D. J. & Dahlquist, F. W. The contact interface of a 120 kD CheA–CheW complex by methyl TROSY interaction spectroscopy. *J. Am. Chem. Soc.* **127**, 9676–9677 (2005).
34. Simon, M. D. et al. The site-specific installation of methyl-lysine analogs into recombinant histones. *Cell* **128**, 1003–1012 (2007).
35. Zhang, X. et al. Structure of the *Neurospora* SET domain protein DIM-5, a histone H3 lysine methyltransferase. *Cell* **111**, 117–127 (2002).
36. Mishima, Y. et al. Hinge and chromoshadow of HP1 $\alpha$  participate in recognition of K9 methylated histone H3 in nucleosomes. *J. Mol. Biol.* **425**, 54–70 (2013).
37. Luger, K., Rechsteiner, T. J. & Richmond, T. J. Preparation of nucleosome core particle from recombinant histones. *Methods Enzymol.* **304**, 3–19 (1999).
38. Dorigo, B. et al. Nucleosome arrays reveal the two-start organization of the chromatin fiber. *Science* **306**, 1571–1573 (2004).
39. Rogge, R. A. et al. Assembly of nucleosomal arrays from recombinant core histones and nucleosome positioning DNA. *J. Vis. Exp.* **79**, 50354 (2013).
40. Delaglio, F. et al. NMRPipe: a multidimensional spectral processing system based on UNIX pipes. *J. Biomol. NMR* **6**, 277–293 (1995).
41. Kato, H. et al. Architecture of the high mobility group nucleosomal protein 2-nucleosome complex as revealed by methyl-based NMR. *Proc. Natl Acad. Sci. USA* **108**, 12283–12288 (2011).
42. Chalmers, M. J. et al. Probing protein ligand interactions by automated hydrogen/deuterium exchange mass spectrometry. *Anal. Chem.* **78**, 1005–1014 (2006).
43. Keppel, T. R. & Weis, D. D. Mapping residual structure in intrinsically disordered proteins at residue resolution using millisecond hydrogen/deuterium exchange and residue averaging. *J. Am. Soc. Mass Spectrom.* **26**, 547–554 (2015).
44. Pascal, B. D. et al. HDX workbench: software for the analysis of H/D exchange MS data. *J. Am. Soc. Mass Spectrom.* **23**, 1512–1521 (2012).
45. Zhang, Z. & Smith, D. L. Determination of amide hydrogen exchange by mass spectrometry: a new tool for protein structure elucidation. *Protein Sci.* **2**, 522–531 (1993).
46. Gamarra, N., Johnson, S. L., Trnka, M. J., Burlingame, A. L. & Narlikar, G. J. The nucleosomal acidic patch relieves auto-inhibition by the ISWI remodeler SNF2h. *eLife* **7**, 34270 (2018).
47. Trnka, M. J., Baker, P. R., Robinson, P. J. J., Burlingame, A. L. & Chalkley, R. J. Matching cross-linked peptide spectra: only as good as the worse identification. *Mol. Cell. Proteomics* **13**, 420–434 (2014).
48. Brown, P. H. & Schuck, P. Macromolecular size-and-shape distributions by sedimentation velocity analytical ultracentrifugation. *Biophys. J.* **90**, 4651–4661 (2006).
49. Brautigam, C. A. Calculations and publication-quality illustrations for analytical ultracentrifugation data. *Methods Enzymol.* **562**, 109–133 (2015).

**Acknowledgements** We thank M. Rosen for sharing data before publication. We thank J. Tretyakova for help and training in histone purification; R. S. Isaac for providing initial nucleosomal array DNA; J. Pelton and the QB3 NMR Facility at the University of California Berkeley for help with collecting and processing NMR data; M. Keenen for providing Pegsilane-coated slides and protocols; C. Stoddard for providing ZMET2; S. Catania and H. Madhani for guidance in *S. pombe* experiments; D. Canzio for help with AUC; the Nikon Imaging Center at UCSF and K. Herrington for training and help with microscope data acquisition. We thank L. Hsieh, N. Gamarra, D. Canzio, A. Larson, E. Nora and H. Madhani for comments on the manuscript and members of the Gross and Narlikar laboratories for discussion. This work was supported by grant NIH NCATS UL1 TRO00004 to S.S., J.D.G. and G.J.N.; Sandler Family Foundation Program for Breakthrough Research Post-doctoral Fellowship to S.S.; NIH NIGMS R01 GM121962 to J.D.G.; NIH R01GM108455 and R35 GM127020 to G.J.N.; PBBR New Frontier Research Award to G.J.N.; Dr. Miriam and Sheldon G. Adelson Medical Research Foundation to A.L.B.; NIH NIGMS P41GM103481 to A.L.B.; Instrumentation Grants- Qexactive Plus (Thermo): NIH S10D016229 to A.L.B., Orbitrap Fusion Lumos (Thermo): University of California, San Francisco (Program for Breakthrough Biomedical Research (PBBR)).

**Author contributions** S.S., J.D.G. and G.J.N. identified and developed the core questions. S.S. performed the bulk of the experiments. V.D. performed HDX-MS experiments and exported the data with the help of B.D.P. M.J.T. performed and analysed XLMS. S.S. and M.J.T. processed HDX-MS raw data. R.W.T. helped with the processing and collection of NMR data. S.S., J.D.G. and G.J.N. wrote the manuscript with contributions from the other authors. G.J.N. and J.D.G. oversaw the project.

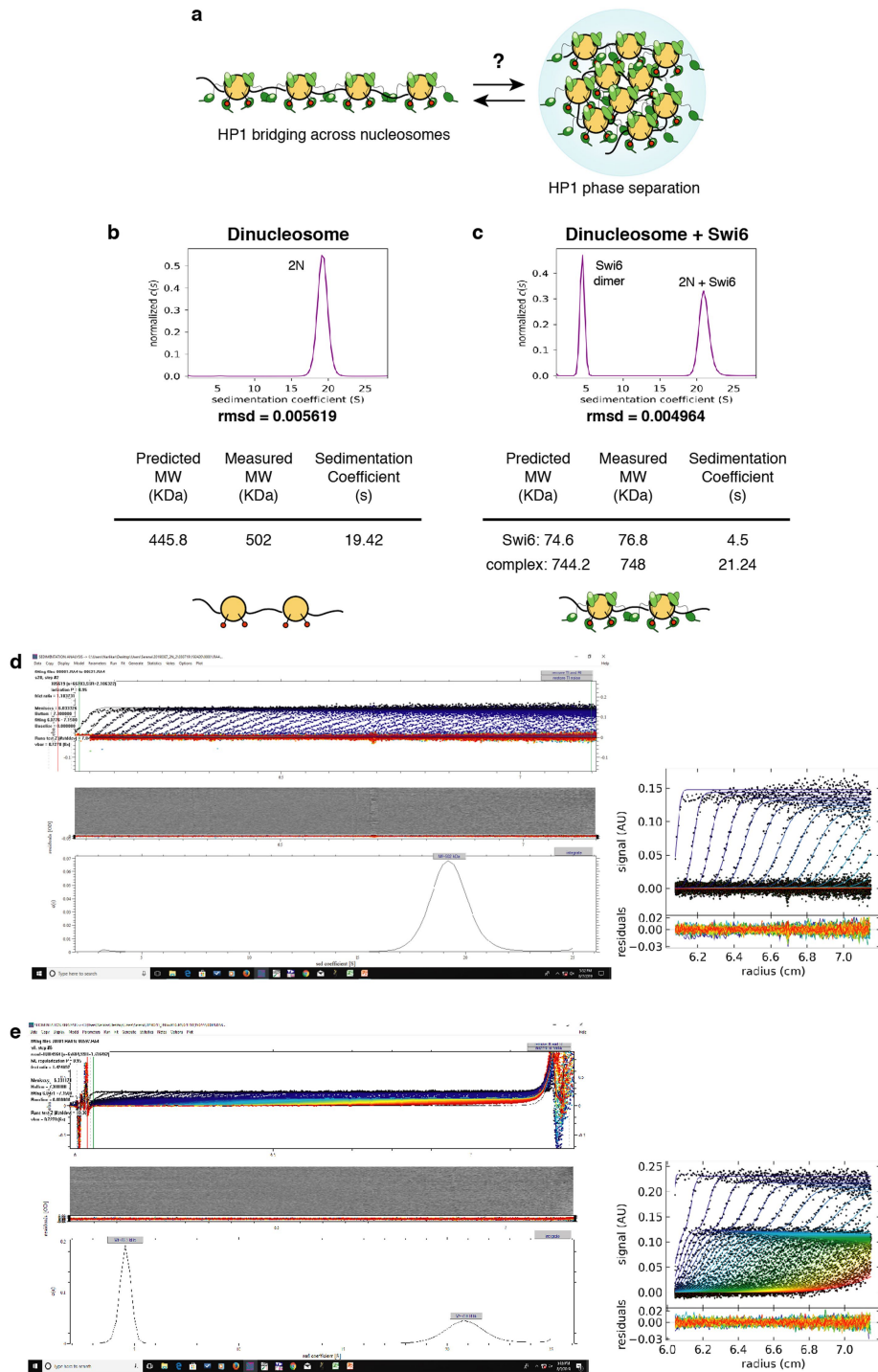
**Competing interests** The authors declare no competing interests.

#### Additional information

**Supplementary information** is available for this paper at <https://doi.org/10.1038/s41586-019-1669-2>.

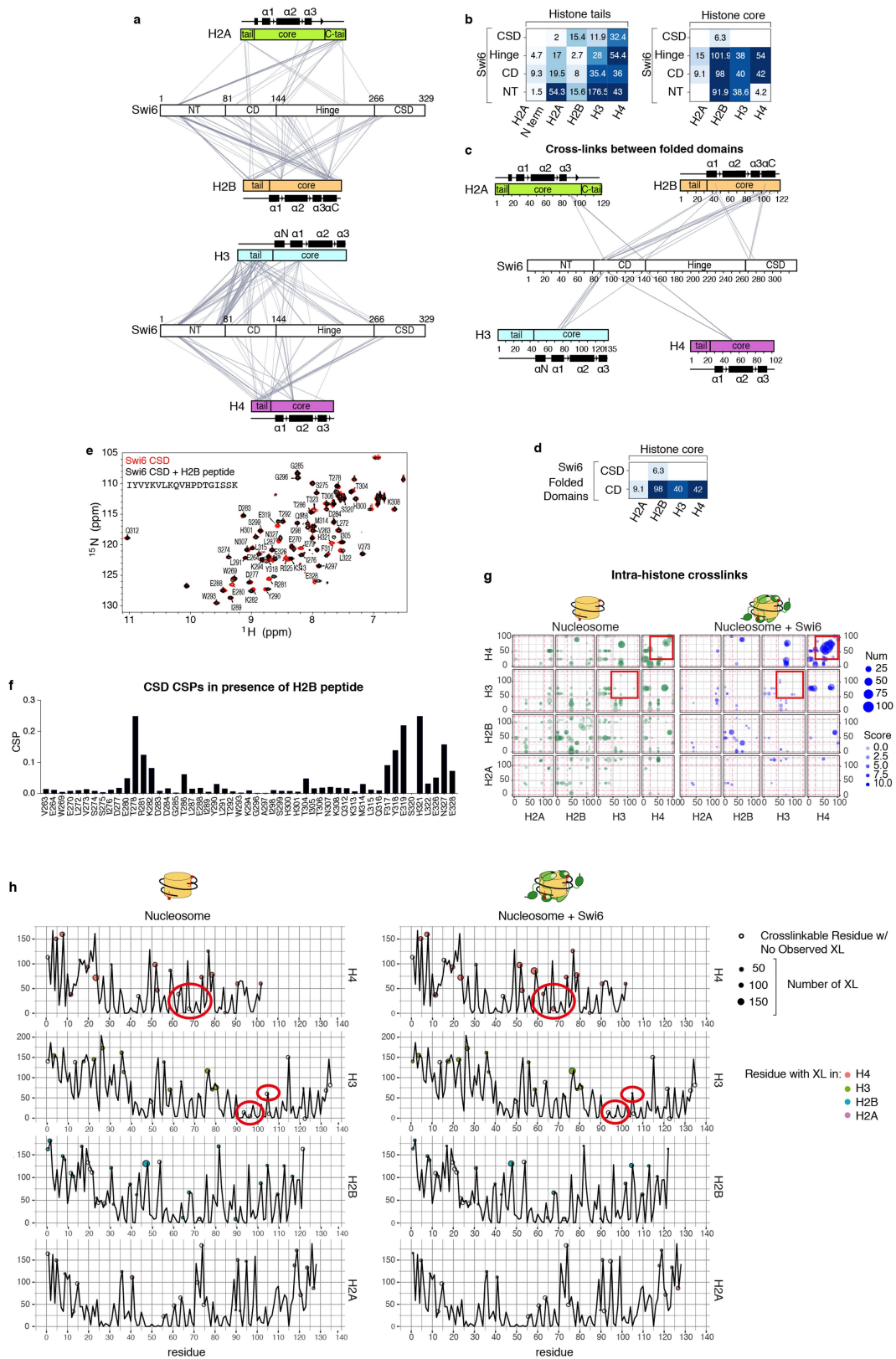
**Correspondence and requests for materials** should be addressed to J.D.G. or G.J.N.

**Reprints and permissions information** is available at <http://www.nature.com/reprints>.



**Extended Data Fig. 1 | Swi6 interaction with chromatin.** **a**, Model for HP1-mediated heterochromatin assembly: the bridging model relies on the ability of HP1 to oligomerize across nucleosomes; the phase separation model relies on the ability of HP1 to form phase-separated assemblies that can sequester chromatin. The molecular link between these two models is unclear. **b**, Sedimentation velocity-analytical ultracentrifugation (SV-AUC) analysis on H3K9me3 dinucleosomes. The continuous sedimentation coefficient distribution ( $c(s)$ ) is shown as a two-dimensional distribution. The measured masses using a continuous function  $c(s)$  distribution versus theoretically

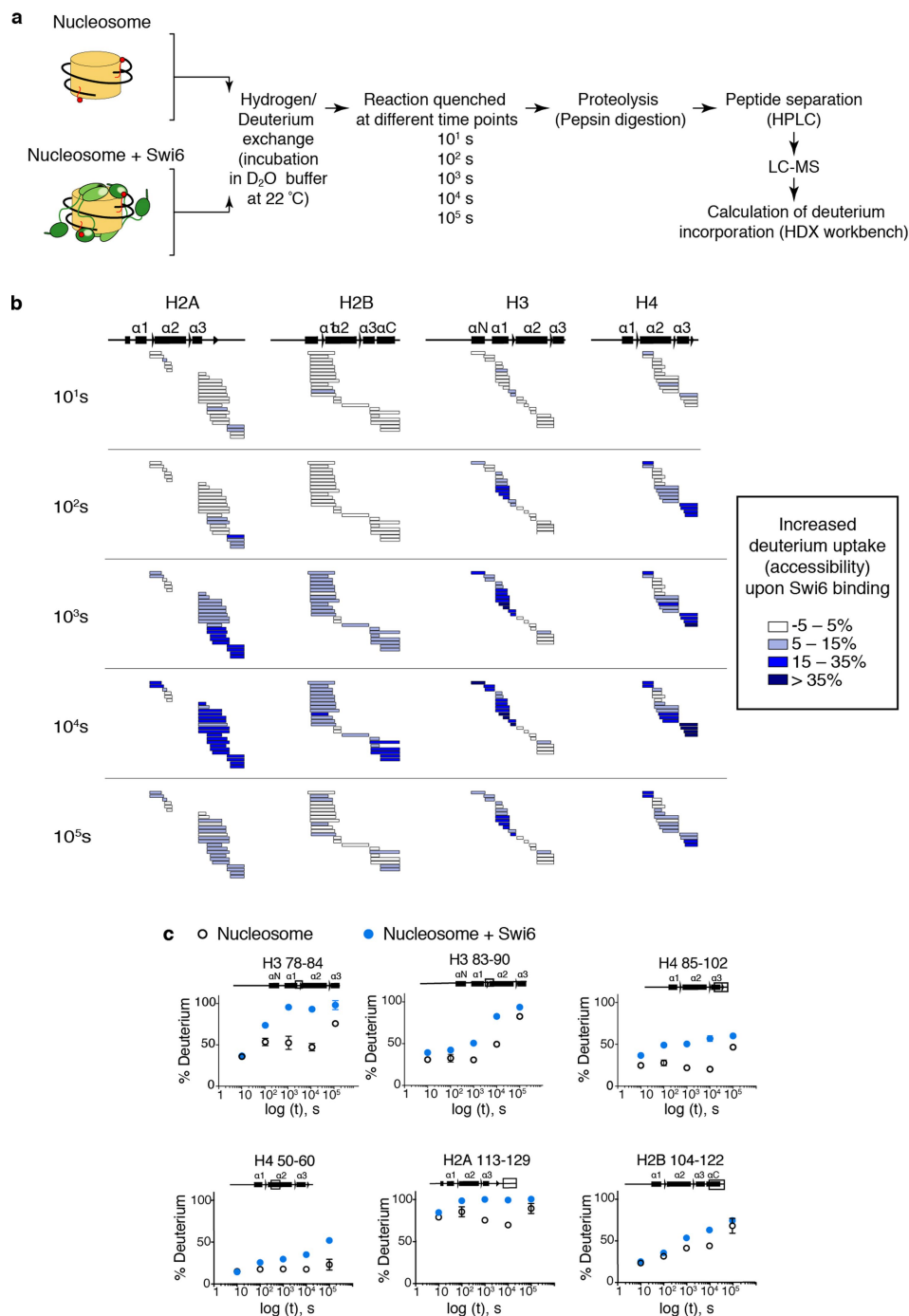
predicted masses are shown. **c**, SV-AUC on H3K9me3 dinucleosomes with Swi6. Data are as in **b**. Analysis is performed using a continuous function  $c(s)$  with a bimodal  $f/f_0$  distribution. The peak at  $s = 21.24$  corresponds to the Swi6-dinucleosome complex. The peak at  $s = 4.5$  corresponds to free Swi6 dimers, as previously shown<sup>4</sup>. **d, e**, Analysis of raw SV-AUC data for dinucleosome alone (**d**) and dinucleosome plus Swi6 complex (**e**) showing that: (i) the fit lines describe the boundary data well; (ii) the r.m.s.d. value is below 0.01; and (iii) the residual bitmap has very few diagonal features indicating the good quality of the fit. For **b-d**, measurements are representative of two independent experiments.



Extended Data Fig. 2 | See next page for caption.

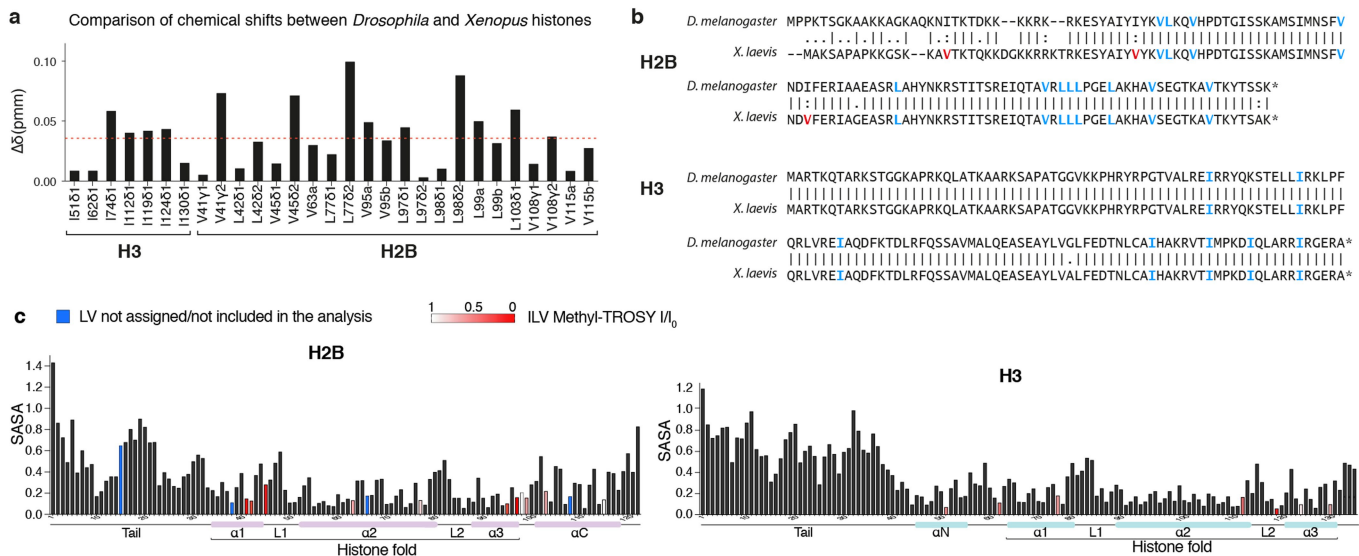
**Extended Data Fig. 2 | Swi6–nucleosome cross-linking analysis.** **a**, EDC cross-linking network between histones and Swi6. Histones tails and core regions are indicated, as well as the different Swi6 domains. **b**, Interactions between Swi6 domains, histone tails and core domains mapped by cross-link spectral counts. The number of cross-linked mass spectra matched to a given domain pair is indicated by the colour of the tile as well as the numbers given. **c, d**, Analysis as in **a** and **b** but performed only on the structured domains of Swi6 (CSD and chromodomain) and on the folded core of histones. **e**, The Swi6 CSD binds to H2B core. Superposition of  $^1\text{H}$ - $^{15}\text{N}$  HSQC spectra of Swi6 CSD with (black) and without (red) H2B peptide. Measurements are representative of three independent experiments. The sequence of the H2B peptide is shown. **f**, Chemical shift perturbation for assigned resonances between Swi6 CSD alone and with the addition of the H2B peptide shown in **e**. **g**, Intra-nucleosome cross-links are altered by Swi6 binding. Each axis maps residue position within a histone, and the red dashed lines indicate the boundaries between histone tail and core domains. A cross-link is represented by a filled circle between two

residues, with area proportional to the number of MS2 spectra identifying a given cross-link. Cross-links found in the free nucleosome state are in green, and cross-links found in the Swi6-bound nucleosome are in blue. The red squares highlight changes in the H3–H3 and H4–H4 cross-linking patterns between the free and bound nucleosome states. **h**, New histone–histone cross-links detected only with Swi6 binding involve buried regions of the nucleosome. The plots report the solvent-accessible surface area (SASA; y axis) versus residues number (x axis) for each histone. Cross-linkable residues (E, D and K) are indicated by a circle. Empty circles represent residues that do not show any cross-linking, and filled circles represent cross-linked residues. The area of the circle reports the number of cross-linked spectra with one peptide mapped to a particular residue. The red ovals highlight buried residues that were observed to cross-link only in the presence of Swi6. Analysis in **a–d, g** and **h** is performed on one of two XLMS datasets. Similar results were obtained with the other dataset that used the BS3 cross-linker.



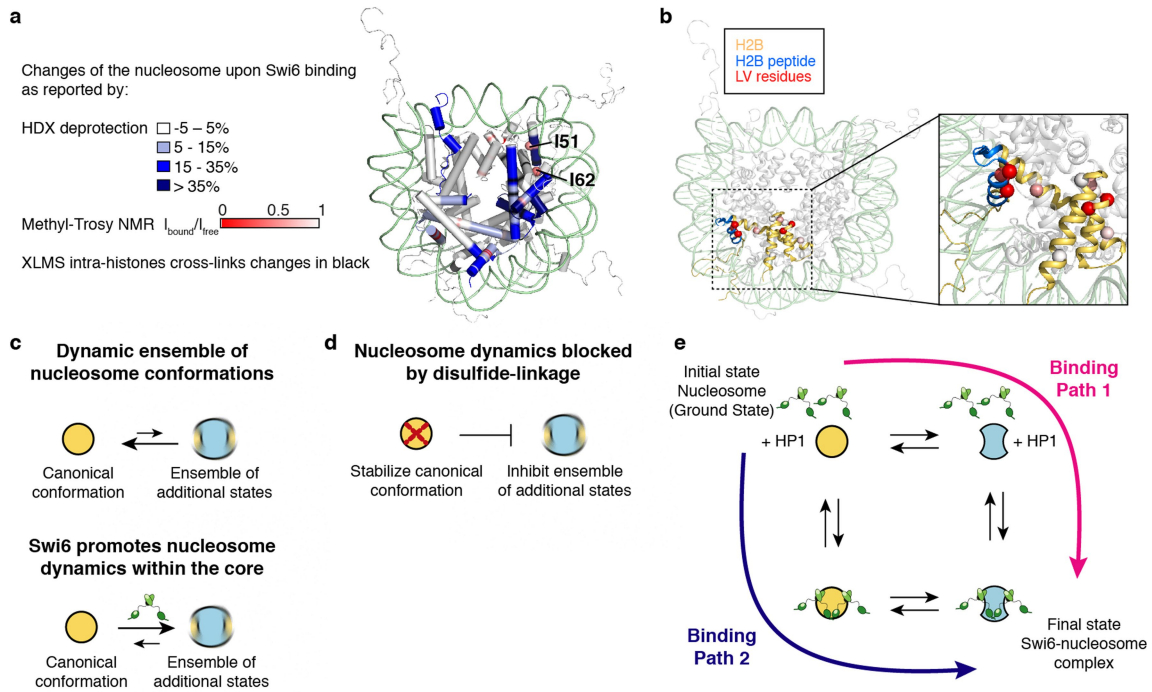
**Extended Data Fig. 3 | HDX-MS with nucleosome-Swi6 complex and nucleosomes alone.** **a**, Experimental scheme for HDX-MS. **b**, Changes in deuterium incorporation are reported for every histone at five different time points. Each horizontal bar represents an individual peptide, and peptides are placed beneath the schematic of secondary structure elements of the histones. Peptides are coloured as specified, showing the mean of deprotection derived from multiple peptides obtained from one of two independent experiments with similar results. Specifically, more than a 35% increase in deuterium incorporation compared to nucleosomes alone is observed in: (i) residues 74–90 of H3, corresponding to a portion of helix  $\alpha 1$  and  $\alpha 2$ , and the connecting loop 1; (ii) residues 48–61 of H3, corresponding to helix  $\alpha N$  of H3; and (iii)

residues 85–102 of H4, corresponding to helix  $\alpha 3$ . Other regions with a marked increase in deuterium uptake are the C-terminal region and helix  $\alpha 2$  of H2A (residues 113–129 and 40–51), the C-terminal of H2B (helix  $\alpha C$ , residues 104–122), and H4 helix  $\alpha 2$  and loop 2 (residues 50–60 and 72–84). These increases in the rates of deuterium incorporation caused by Swi6 binding indicate extensive changes in the backbone hydrogen bonding of histones within the nucleosome and partial unfolding of the helices in the histones. **c**, Kinetics of deuterium uptake of example histone peptides (residue numbers indicated) over the time course. Data are mean and s.d. of multiple peptides obtained from one of two independent experiments with similar results. Error bars not shown for points when shorter than the height of the symbol.



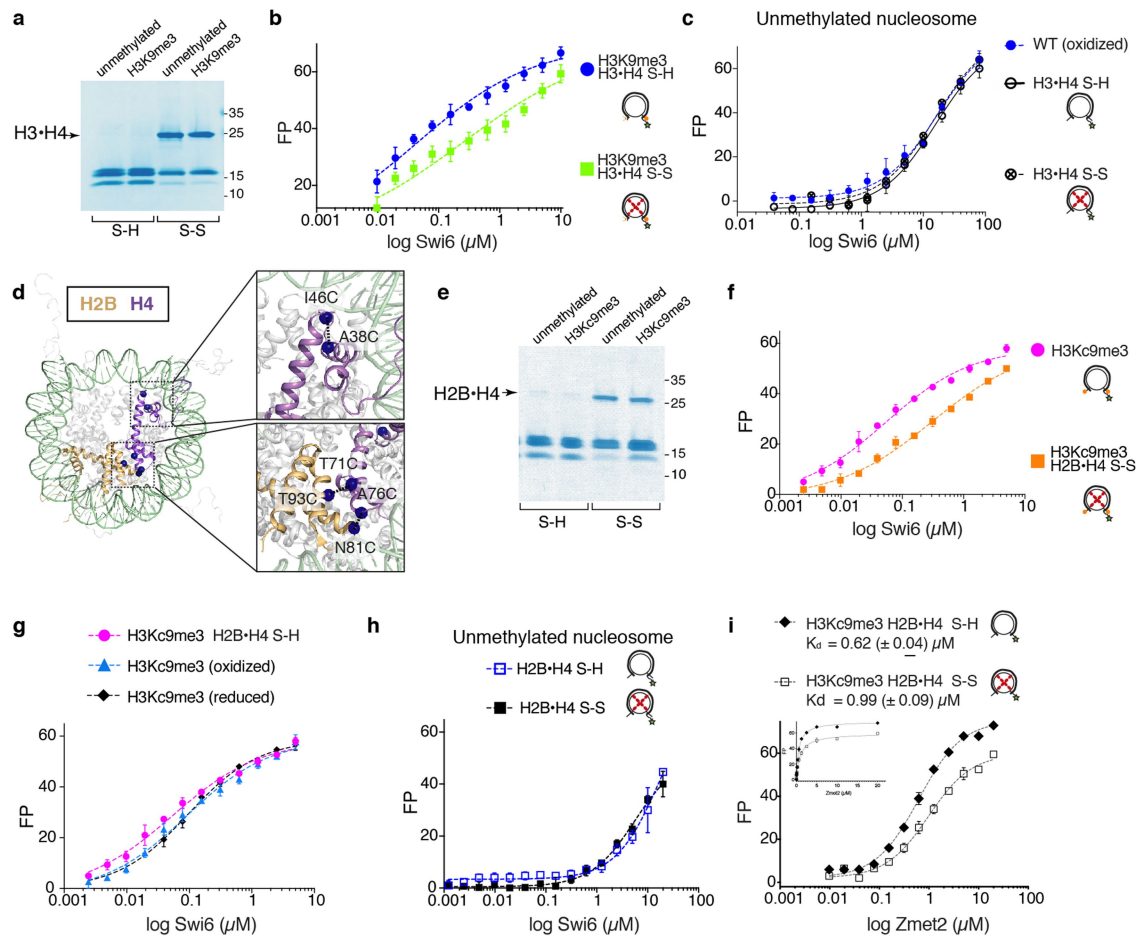
**Extended Data Fig. 4 | Nucleosome methyl-TROSY NMR.** **a**, The methyl-TROSY spectra of H3 and H2B are well resolved and the chemical shift differences between the cross-peaks of our spectra and of the published spectra of *Drosophila* nucleosomes are small (less than 0.1 ppm)<sup>41</sup>. Owing to these small changes and the high protein conservation between the two species, we were able to transfer the assignments to all the cross-peaks of H3 and most of the cross-peaks of H2B. The chemical shift change ( $\Delta\delta$ ) plot reports the differences in chemical shift of the cross-peaks for conserved Ile, Leu and Val (ILV) residues in *Drosophila* and *Xenopus* histones.  $\Delta\delta$  values were calculated from the equation:  $\sqrt{0.5((\delta H_{Drosophila} - \delta H_{Xenopus})^2 + (0.2(\delta C_{Drosophila} - \delta C_{Xenopus}))^2)}$  in which the factor of 0.2 is used as a scaling factor for the carbon spectral width. The average  $\Delta\delta$  value is shown as a red dashed line. Experiments were performed twice to optimize conditions; data from one experiment are reported. **b**, Amino

acid sequence alignment of *Drosophila* and *Xenopus* H2B and H3 histones. ILV residues conserved between the two species are coloured in blue, and non-conserved ILV residues are in red. Ile residues are fully conserved between H3 histones. Leu and Val are conserved between H2B histones, except for V15, V38 and V66, which are present only in the *Xenopus* histone. V15, V38 and V66 are not included in our NMR analysis. **c**, Quantification of the SASA of the residues indicated (x axis) in histone H2B (left) and H3 (right). The SASA was calculated from the PDB structure file 1KX5 using the program POPS. The SASA values are for the entire residue and represent fraction of exposed surface area. Bars corresponding to ILV residues are coloured in red with shading as specified, reflecting changes reported from the methyl-TROSY experiments due to Swi6 binding. ILV residues not assigned or not included in the analysis are in blue. The schematic of secondary structure elements is shown below the x axis.



**Extended Data Fig. 5 | Swi6 disorganizes the nucleosome core.** **a**, Mapping of the Swi6-induced changes in the nucleosome structure (PDB code 1KX5), as detected by XLMS (Fig. 1), HDX-MS (Fig. 2), and methyl-TROSY NMR (Fig. 3). H3 residues I51 and I62 are shown as spheres. The figure highlights how the three different techniques consistently reported alterations in the same regions of the octamer. **b**, In the nucleosome crystal structure, H2B is coloured in light orange, H2B peptide used in the CSD  $^1\text{H}$ - $^{15}\text{N}$  HSQC NMR experiment is in cyan and Leu and Val residues analysed in the nucleosome methyl-TROSY NMR are represented as spheres and coloured according to the extent of broadening determined by  $I_{\text{bound}}/I_{\text{free}}$ . The magnified panel shows the location of the H2B peptide tested for binding to the CSD. **c**, Model depicting the effect of Swi6 on nucleosome conformations. Nucleosomes in solution can sample an ensemble of conformational states, of which the canonical conformation observed in the crystal structure is the most populated and lowest energy state. Swi6 increases nucleosome dynamics and promotes nucleosomes alternative states. Top, in

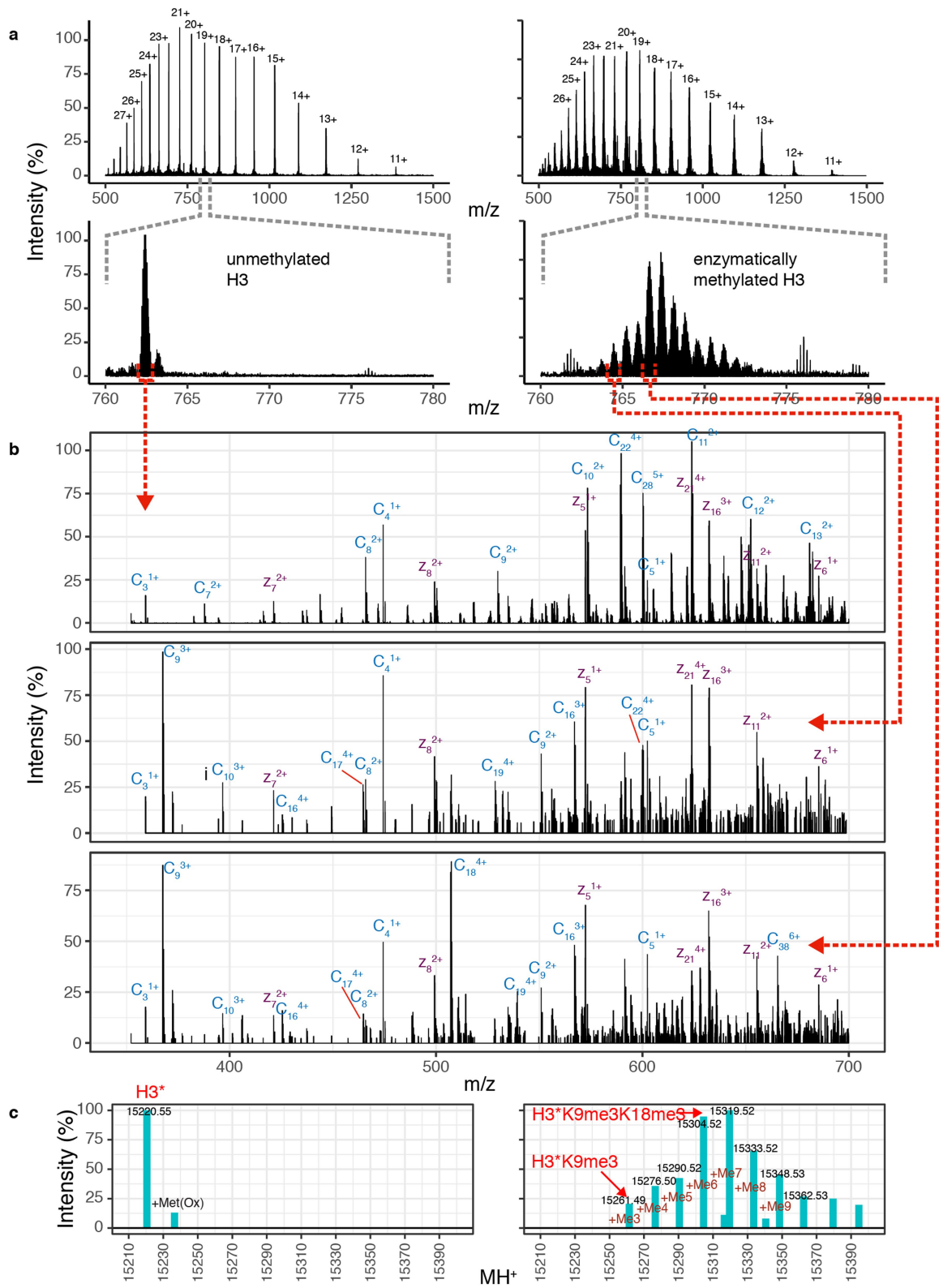
the absence of Swi6, the equilibrium is pushed towards the nucleosome in the canonical state. Bottom, Swi6 increases nucleosome dynamics and promotes formation of a larger ensemble of nucleosomal conformations. **d**, Model of how disulfide cross-links in the nucleosome core prevent nucleosome core dynamics. **e**, This thermodynamic cycle integrates the different states of the nucleosome and nucleosome-Swi6 complexes implied by our work. In this thermodynamic cycle, the overall process involves a thermodynamic coupling between Swi6 binding and increased nucleosome dynamics. Path 1 shows how the intrinsic equilibrium between static and dynamic nucleosome states can be driven towards a dynamic nucleosomal state by Swi6 binding, and path 2 shows how binding by Swi6 to a static nucleosome can drive the equilibrium of the Swi6-nucleosome complex towards a more dynamic nucleosome state. Both paths lead to the same final state where the conformation of the Swi6-bound nucleosome is different from the one observed in the crystal structure (PDB code 1KX5). Importantly, both paths are thermodynamically equivalent.



### Extended Data Fig. 6 | Nucleosome octamer dynamics are important for Swi6 nucleosome binding.

**a**, Representative non-reducing SDS-PAGE showing nucleosome with H3-H4 histone disulfide-linked (H3•H4 S-S) or reduced (H3•H4 S-H). Around 90% of H3 and H4 are disulfide-linked in both the methylated and unmethylated nucleosomes. These are the cross-linking sites used in Fig. 4. For gel source data, see Supplementary Fig. 1. **b**, Nucleosome binding assays by fluorescence anisotropy showing reduced binding of Swi6 to H3K9me3 nucleosomes containing H3-H4 disulfide-linked octamer (H3•H4 S-S) versus H3•H4 S-H. **c**, Fluorescence anisotropy measuring Swi6 binding to unmethylated nucleosome, H3•H4 S-H and S-S, showing that disulfide linkages have no effect on Swi6 binding to unmethylated nucleosome. **d**, Additional residues in the H2B and H4 mutated to Cys for generating dynamically restrained octamers are represented with spheres. **e**, Representative non-reducing SDS-PAGE showing nucleosome with H2B-H4 histone disulfide-linked (H2B•H4 S-S) or reduced (H2B•H4 S-H). Around 50% of H2B and H4 are

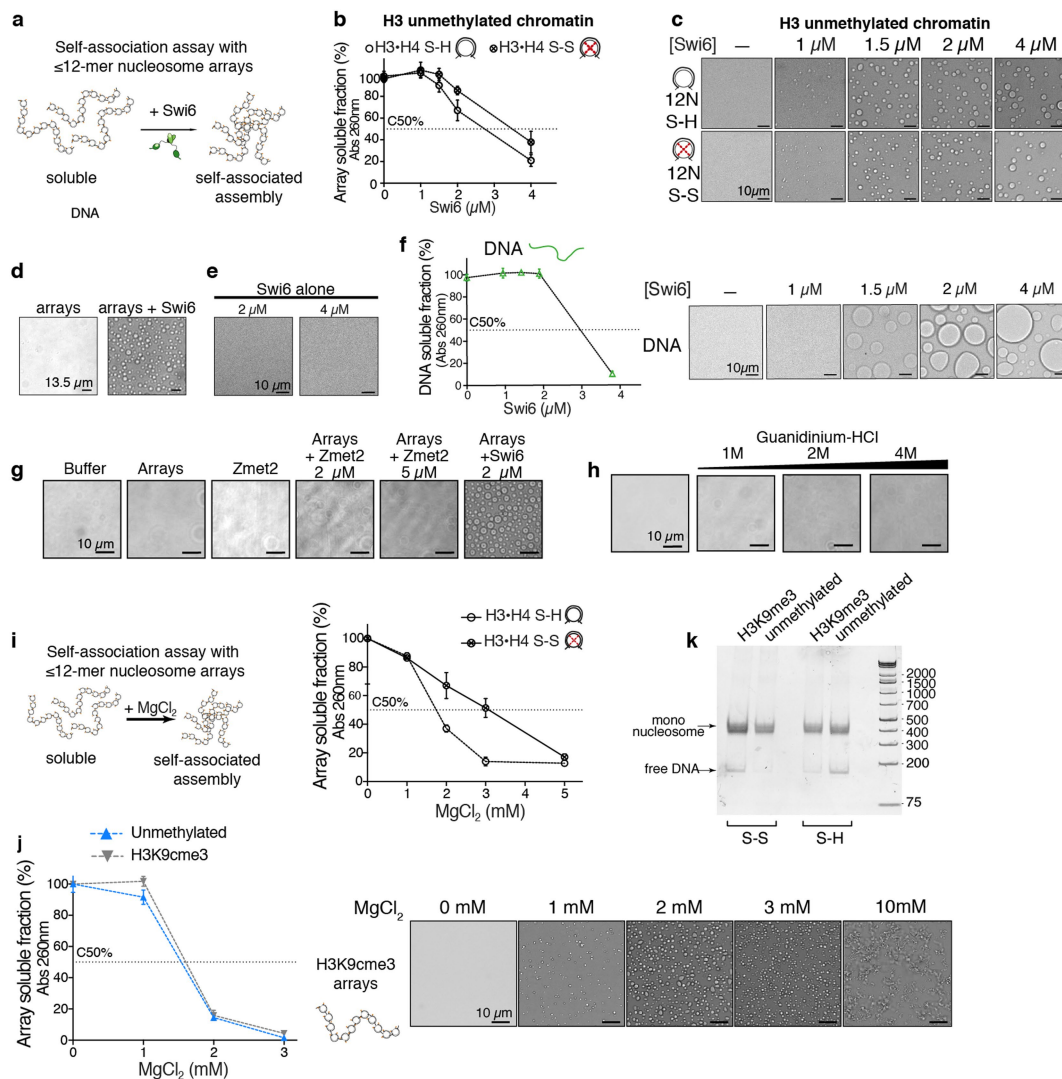
disulfide-linked in both H3K9me3 and unmethylated nucleosomes. For gel source data, see Supplementary Fig. 1. **f**, Nucleosome binding assays by fluorescence anisotropy showing reduced binding of Swi6 to H2B-H4 disulfide-linked octamer (H2B•H4 S-S). **g**, Fluorescence anisotropy experiments showing comparable Swi6 binding to H3K9me3 non-oxidized, H3K9me3 oxidized and H2B•H4 S-H mononucleosomes. These results show that the oxidation process does not alter Swi6 binding to Cys-devoid nucleosomes and that the presence of reduced Cys does not affect Swi6 binding either. **h**, Fluorescence anisotropy measuring Swi6 binding to unmethylated nucleosome, H2B•H4 S-H and S-S, showing that disulfide linkages have no effect on Swi6 binding to unmethylated nucleosomes. **i**, Nucleosome binding assays by fluorescence anisotropy showing that Zmet2 binding to H2B-H4 disulfide-linked octamer (H2B•H4 S-S) is not significantly affected. FP, fluorescence polarization units. Measurements entailed at least three independent experiments and error bars reflect s.d.



Extended Data Fig. 7 | See next page for caption.

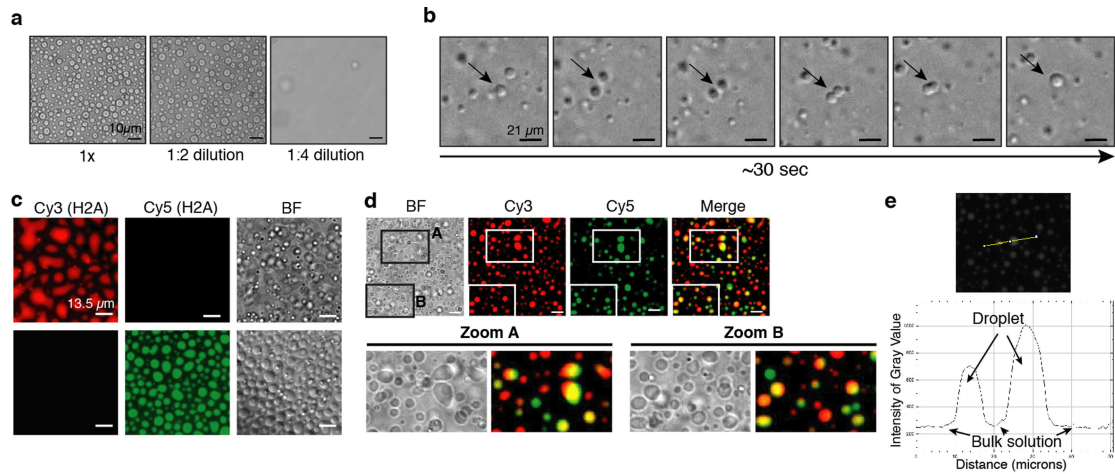
**Extended Data Fig. 7 | Characterization of H3 enzymatic methylation by Dim5.** Methylation of H3 was followed by EST-based LC-MS/MS analysis of the intact proteins. **a**, Charge state envelope of untreated (left) and methylated (right) H3. The bottom panel, focused on a single charge state, shows disappearance of the starting material and the formation of higher mass species, spaced 14 Da apart. **b**, ETD-based mass spectrometry of precursor ions corresponding to unmethylated H3 (top), H3K9me3 (middle) and H3K9me3-K18me3 (bottom). The rationale for these assignments is based on the precursor mass values and by the product ions. The z-ions (purple) do not change between the three spectra, whereas the pattern of c-ions (blue) are mass shifted by 42 Da and charge-state shifted by 1+ at C9 between the top and middle or bottom panels, and again at C18 between the middle and bottom

panels. These assignments are further validated by bottom-up proteomics analysis of Lys-C-digested samples (not shown). **c**, The precursor ion spectra in **a** were deconvoluted using Xtract, which models both the charge states and the isotope distributions. Deconvoluted  $MH^+$  values are consistent with multiple methylation states (owing to the difficulty of modelling isotope distributions from large proteins, particularly as there is some underlying oxidation, Xtract sometimes picks the wrong monoisotope). Deconvoluted intensities show that the enzymatically treated sample (right) contains no notable unmethylated H3 or mono- and di-methylated H3K9. Although 100% of analysed sample is tri-methylated at H3K9, additional methylations occur at H3K18 as noted above. The sample analysed here was used to carry out all the experiments to minimize variability.



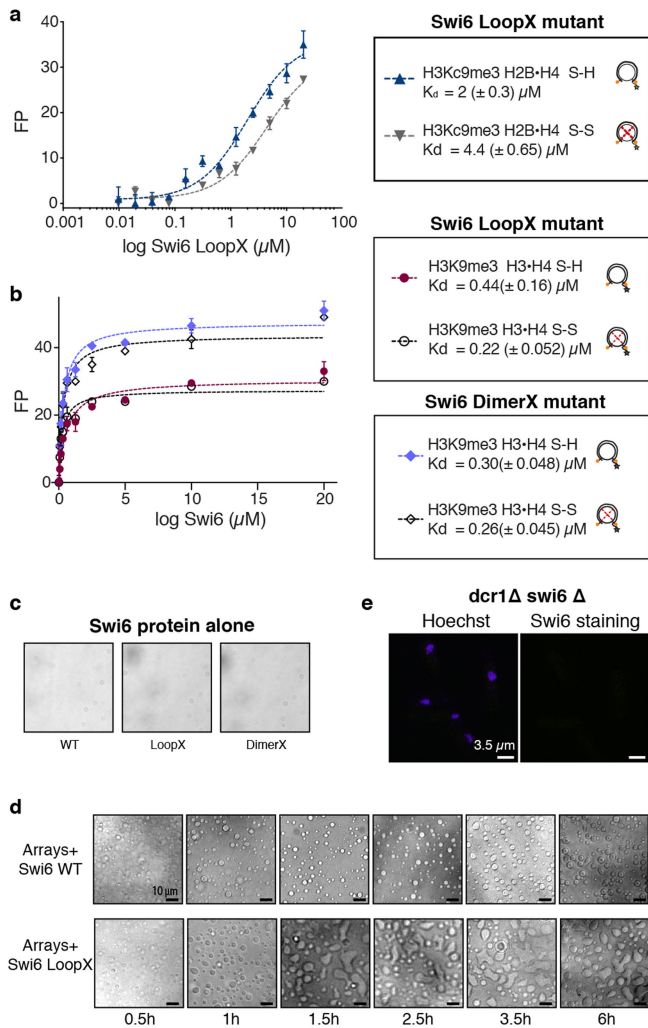
**Extended Data Fig. 8 | Nucleosome disorganization and chromatin phase separation are specifically driven by Swi6.** **a**, Schematic of chromatin self-association assay. **b, c**, Restraining octamer dynamics do not affect the condensation of unmethylated chromatin in liquid droplets. Self-association assays in **b** are performed with unmethylated nucleosome arrays containing H3•H4 S-S (oxidized) and H3•H4 S-H (reduced) octamers as a function of increasing concentration of Swi6. In **c**, bright-field representative images of the array-Swi6 complex analysed in **b** show that the formation of phase-separated droplets is not affected by the disulfide linkages in absence of H3K9me3. **d**, Swi6 induces chromatin condensation in liquid droplets at physiological conditions—150 mM KCl, 30 °C, 2 μM Swi6. Bright-field representative images. **e**, Swi6 alone does not form phase-separated liquid droplets. Bright-field representative images of the Swi6 alone. **f**, Left, self-association assay performed with naked DNA (601 × 12, approximately 2 kb) in presence of increasing concentrations of Swi6. Right, bright-field representative images of the DNA-Swi6 complex analysed in the left panel, showing the formation of phase-separated droplets. **g**, Zmet2 does not form phase-separated assemblies alone and it does not promote chromatin condensation in liquid droplets.

Experiments are done at 40 nM nucleosome arrays, with 2 and 5 μM of Zmet2. Bright-field images of buffer only and Swi6-chromatin droplets are shown as controls. **h**, Titration of the denaturant guanidinium-HCl into nucleosome arrays does not promote formation of phase-separated droplets, which indicates that Swi6 specifically disorganizes the nucleosome core. **i**, Disulfide cross-links between H3 and H4 impair Mg<sup>2+</sup>-driven self-association of nucleosome arrays, indicating the role of nucleosome core dynamic for inter-nucleosome interactions. **j**, Left, Mg<sup>2+</sup>-driven self-association of unmethylated and H3K9cme3 arrays are comparable. Right, representative bright-field images of the H3K9cme3 array sedimentation analysed in the left panel, showing the formation of rounded phase-separated condensates at 2 and 3 mM Mg<sup>2+</sup>. The assay is performed in TE 0.1 (10 mM Tris pH 7.8, 0.1 mM EDTA) and 75 mM KCl. **k**, Nucleosome arrays quality controls, showing comparable octamer saturation and absence of over- and under-assemblies. Arrays are digested with HpaI, run on a native acrylamide gel, and DNA is stained. For source gel data, see Supplementary Fig. 1. All arrays used in this study conformed to the quality standard shown in **k**. In **b-i** and **j**, measurements and images entailed three independent experiments; error bars reflect s.d.



**Extended Data Fig. 9 | Swi6-chromatin assemblies present liquid-like properties.** **a**, Chromatin-Swi6 condensates are reversible after dilution. **b**, Chromatin-Swi6 droplets fuse within seconds after incubation. The time course depicted is 30 s. **c**, Chromatin is included in Swi6-induced condensates. Nucleosome arrays are assembled with H2A-Cy3 or H2A-Cy5 and H3K9me3 octamers. Images showing Cy3- or Cy5-labelled chromatin mixed with Swi6 separately, before being incubated together. **d**, Images show condensates 30 min after mixing Cy3 and Cy5 pre-formed droplets. By around 1 h, most of

the droplets contain homogeneous labelling with both dyes. Doubly labelled droplets indicate chromatin exchanges between the pre-formed condensates. **e**, Quantification of fluorescence intensity done in ImageJ using the Plot Profile function that creates a plot of intensity values across the yellow line shown in the left panel. Higher octamer concentration within the droplets as compare to the bulk of the solution is detected. Images are representative images from at least three independent experiments.



**Extended Data Fig. 10 | Swi6 dimerX and loopX mutants are defective in promoting octamer distortion and forming heterochromatin foci in *S. pombe*.** **a**, Nucleosome binding assays by fluorescence anisotropy showing that binding of Swi6 loopX mutant to H3K9me3 nucleosomes is not affected by H2B-H4 histone disulfide linkage. H2B-H4 S-S are oxidized nucleosome, H2B-H4 S-H are reduced nucleosomes.  $K_d$  values are shown. **b**, Nucleosome binding assays by fluorescence anisotropy showing that binding of the Swi6 loopX and dimerX mutants to H3K9me3 nucleosomes is not affected by H3-H4 histone disulfide linkage. H3-H4 S-S are oxidized nucleosome, H3-H4 S-H are reduced nucleosomes.  $K_d$  values are shown. **c**, Wild-type Swi6 and loopX and dimerX mutant Swi6 proteins do not form liquid droplets in absence of chromatin (Swi6 concentration is 4  $\mu\text{M}$ ). **d**, Bright-field images showing droplet wetting over time. Swi6-chromatin condensates are incubated at room temperature and images are collected at the indicated times. Condensates are imaged on a bottom glass plate coated with Peg-silane (see Methods). **e**, Swi6 immunofluorescence on *dcr1Δ swi6Δ S. pombe* cells shows absence of Swi6 staining, confirming the specificity of the anti-Swi6 antibody. Images in **c-e** are representative of at least three independent experiments. In **a** and **b**, measurements entailed three independent experiments; error bars denote s.d.

## Reporting Summary

Nature Research wishes to improve the reproducibility of the work that we publish. This form provides structure for consistency and transparency in reporting. For further information on Nature Research policies, see [Authors & Referees](#) and the [Editorial Policy Checklist](#).

### Statistics

For all statistical analyses, confirm that the following items are present in the figure legend, table legend, main text, or Methods section.

- |     |           |
|-----|-----------|
| n/a | Confirmed |
|-----|-----------|
- The exact sample size ( $n$ ) for each experimental group/condition, given as a discrete number and unit of measurement
  - A statement on whether measurements were taken from distinct samples or whether the same sample was measured repeatedly
  - The statistical test(s) used AND whether they are one- or two-sided  
*Only common tests should be described solely by name; describe more complex techniques in the Methods section.*
  - A description of all covariates tested
  - A description of any assumptions or corrections, such as tests of normality and adjustment for multiple comparisons
  - A full description of the statistical parameters including central tendency (e.g. means) or other basic estimates (e.g. regression coefficient) AND variation (e.g. standard deviation) or associated estimates of uncertainty (e.g. confidence intervals)
  - For null hypothesis testing, the test statistic (e.g.  $F$ ,  $t$ ,  $r$ ) with confidence intervals, effect sizes, degrees of freedom and  $P$  value noted  
*Give  $P$  values as exact values whenever suitable.*
  - For Bayesian analysis, information on the choice of priors and Markov chain Monte Carlo settings
  - For hierarchical and complex designs, identification of the appropriate level for tests and full reporting of outcomes
  - Estimates of effect sizes (e.g. Cohen's  $d$ , Pearson's  $r$ ), indicating how they were calculated

*Our web collection on [statistics for biologists](#) contains articles on many of the points above.*

### Software and code

Policy information about [availability of computer code](#)

Data collection NIS-Elements AR version 5.11, TopSpin 1.2 and 1.3, ZEN blue pro v2.5.

Data analysis Coot 0.8.7, NMRPipe 8.9, NMRFAM-SPARKY 1.2, Mascot (Matrix Science) 2.3.01, HDX Workbench 3.1, Proteome Discoverer 1.4, Protein Prospector 5.17.2, Graph Pad Prism V7 (GraphPad Software), ImageJ 1.51s, SEDNTERP 20130813beta, Gussi 1.0.2, Sedfit 12.3.

For manuscripts utilizing custom algorithms or software that are central to the research but not yet described in published literature, software must be made available to editors/reviewers. We strongly encourage code deposition in a community repository (e.g. GitHub). See the Nature Research [guidelines for submitting code & software](#) for further information.

### Data

Policy information about [availability of data](#)

All manuscripts must include a [data availability statement](#). This statement should provide the following information, where applicable:

- Accession codes, unique identifiers, or web links for publicly available datasets
- A list of figures that have associated raw data
- A description of any restrictions on data availability

XLMS data that support the finding of this study are available using MS viewer at <http://msviewer.ucsf.edu/prospector/cgi-bin/msform.cgi?form=msviewer> Using the search key: 9ojpmsdzk5.  
HDX-MS raw data and NMR peak lists are available on request from the corresponding authors GJN and JDG.  
The rest of the relevant data are included in the paper and extended data files.

## Field-specific reporting

Please select the one below that is the best fit for your research. If you are not sure, read the appropriate sections before making your selection.

Life sciences  Behavioural & social sciences  Ecological, evolutionary & environmental sciences

For a reference copy of the document with all sections, see [nature.com/documents/nr-reporting-summary-flat.pdf](https://www.nature.com/documents/nr-reporting-summary-flat.pdf)

## Life sciences study design

All studies must disclose on these points even when the disclosure is negative.

Sample size	At least three independent experiments are performed to calculate mean and SD. For immunostaining, cell sample size was chosen so that it would reflect the overall population (increasing of sample size did not affect the result).
Data exclusions	No data were excluded.
Replication	Binding, pelleting and in vivo experiments were repeated so that our data are based on at least three independent experiments with consistent results. The precise number of repeats are given in the figure legend. Nucleosome methyl-TROSY experiments were performed two times to optimize conditions, data from one experiment are reported in the study. XLMS was performed on two independent samples using two different cross-linkers with similar results and only one data set is reported in the manuscript. HDX-MS experiments were performed two time with consistent results.
Randomization	We did not use randomization, because our work does not involve clinical trials or population studies.
Blinding	Blinding did not applied to this study as no group allocation was performed.

## Reporting for specific materials, systems and methods

We require information from authors about some types of materials, experimental systems and methods used in many studies. Here, indicate whether each material, system or method listed is relevant to your study. If you are not sure if a list item applies to your research, read the appropriate section before selecting a response.

### Materials & experimental systems

n/a	Involved in the study
<input type="checkbox"/>	<input checked="" type="checkbox"/> Antibodies
<input type="checkbox"/>	<input checked="" type="checkbox"/> Eukaryotic cell lines
<input checked="" type="checkbox"/>	<input type="checkbox"/> Palaeontology
<input checked="" type="checkbox"/>	<input type="checkbox"/> Animals and other organisms
<input checked="" type="checkbox"/>	<input type="checkbox"/> Human research participants
<input checked="" type="checkbox"/>	<input type="checkbox"/> Clinical data

### Methods

n/a	Involved in the study
<input checked="" type="checkbox"/>	<input type="checkbox"/> ChIP-seq
<input checked="" type="checkbox"/>	<input type="checkbox"/> Flow cytometry
<input checked="" type="checkbox"/>	<input type="checkbox"/> MRI-based neuroimaging

## Antibodies

Antibodies used	Anti-Swi6 rabbit antibody previously generated in the lab (dilution 1:500). Goat anti-Rabbit Alexa 488, Invitrogen # A32731 (dilution 1:1000).
Validation	Swi6 antibody was previously used and validated in Canzio et al. 2013 by Western Blot and ChIP. Immunofluorescence validation done by probing cells lacking Swi6, as shown in Extended Data Fig. 10e.

## Eukaryotic cell lines

Policy information about [cell lines](#)

Cell line source(s)	S. pombe strains used in this study are described in Canzio et al. 2013: PM0251: P(h+), ura4-DS/E, ade6-M210, leu1-32, imr1L(Ncol)::ura4, otr1R(Sph1)::ade6 DC27: PM0251, swi6Δ::KanMX::KanMX, dcr1Δ::NatMX DC30: PM0251, swi6::KanMX::KanMX, dcr1Δ::NatMX DC32: PM0251, swi6 (R93A-K94A)::KanMX::KanMX, dcr1Δ::NatMX
Authentication	Cells were previously authenticated in the Narlikar lab as described in Canzio et al. 2013 by Western blot, ChIP and genotyping, and confirmed by immunostaining in this study.

Mycoplasma contamination

Cells were not tested for mycoplasma contamination.

Commonly misidentified lines  
(See [ICLAC](#) register)

No commonly misidentified cell lines were used.